

Restoration of the K and F Components of the Solar Corona from LASCO-C2 Images over 24 Years [1996 – 2019]

Antoine Llebaria¹ · Philippe Lamy²●● ·
Hugo Gilardy² · Brice Boclet¹ · Jean Loirat¹

© Springer ●●●●

Abstract We present a photometrically accurate restoration of the K- and F-coronae from white-light images obtained over 24 years [1996–2019] by the *Large-Angle Spectrometric COronagraph* (LASCO-C2) onboard the *Solar and Heliospheric Observatory* (SOHO). The procedure starts with the data set of unpolarized images of 512×512 pixels produced by the polarimetric analysis of the routine C2 polarization sequences (Lamy et al. *Solar Phys.* **295**, 89, 2020) in which the F-corona, the instrumental stray light, and possible remnants of the K-corona due to the imperfect polarimetric separation are entangled. Disentangling these components requires a complex procedure organized in three stages, each composed of several steps. Stage 1 establishes the distinct variations of the radiance of these components with the Sun–SOHO distance, and generate a new data set of median images calculated for each Carrington rotation. Stage 2 achieves the restoration of a set of 36 stray-light images that account for the temporal variation of the stray-light pattern, in particular those associated with the periodic roll maneuvers of SOHO which started in 2003. Stage 3 achieves

✉ P. Lamy
philippe.lamy@latmos.ipsl.fr
A. Llebaria
a.llebaria@laposte.net
H. Gilardy
hugo.gilardy@latmos.ipsl.fr
B. Boclet
bricexp@hotmail.com
J. Loirat
jean.loirat@gmail.com

¹ Laboratoire d’Astrophysique de Marseille, CNRS & Aix-Marseille Université, 38 rue Frédéric Joliot-Curie, 13388 Marseille cedex 13, France

² Laboratoire Atmosphères, Milieux et Observations Spatiales, CNRS & UVSQ, 11 Bd d’Alember, 78280 Guyancourt, France

the restoration of the F-corona, and a time series of daily images is generated. Combining these images with the set of stray-light images allowed us to process the whole set of routine LASCO-C2 images of 1024×1024 pixels (approximately 626,000 images) and to produce calibrated, high-resolution images of the K-corona. The two sets of images of the K-corona, that produced by polarimetric separation of 512×512 pixels images and that presently produced by subtraction, are in excellent photometric agreement. We extend our past conclusions that the temporal variation of the integrated radiance of the K-corona tracks the solar activity over Solar Cycles 23 and 24, and that it is highly correlated with the temporal variation of the total magnetic field. The behaviours of the integrated radiance during the last few years of the declining phases of Solar Cycles 23 and 24 are remarkably similar, reaching the same base level and leading to a duration of 11.0 years for the latter cycle, in agreement with that derived from sunspots.

Keywords: Corona, F-corona, K-corona, Stray light

1. Introduction

Most of the analyses published so far of the white-light images obtained with the *Large-Angle Spectrometric COronagraph* (LASCO-C2: Brueckner et al., 1995) of the *Solar and Heliospheric Observatory* (SOHO: Domingo, Fleck, and Poland, 1995) relied on the subtraction of simple empirical background images to reveal the dynamic features of the K-corona such as coronal mass ejections (CMEs). These background images are constructed by taking the minimum of the daily median images over a period of typically one month so that the daily median eliminates the short-term changes and the monthly minimum eliminates the longer-term changes. This technique, as well as others such as running- or base-differences, removes the static component of the images, which comprises the F-corona, the stable background K-corona, and any instrumental stray light. It was however applied by Battams et al. (2020) to build a coronal brightness index, but the authors admitted that it does remove some amount of K-corona signal “primarily in persistent streamers in equatorial latitudes and most noticeably around periods of low solar activity”. In summary, these techniques are appropriate to the qualitative and even quantitative analysis of dynamic structures (e.g. CMEs), but questionable for analysis that require accurate quantitative determinations of the F-corona and the global K-corona, which both requires a rigorous restoration.

The very first attempt to build a time series of K-corona images (from March 1996 to January 1999) was performed by Llebaria, Lamy, and Koutchmy (1999) for the purpose of studying coronal activity. They did not elaborate their procedure in their short article, but underlined the complexity of separating the three components present in the LASCO-C2 images: K-corona, F-corona, and stray light. They further pointed out the importance of taking into account the eccentricity of the orbit of the SOHO spacecraft as well as its inclination with respect to the plane of symmetry of the zodiacal cloud crossed twice per year by SOHO.

The difficulties are well illustrated by the work of Hayes, Vourlidas, and Howard (2001) who endeavored to derive the electron density from the inversion of LASCO-C2 total brightness images. Their attempt to subtract the F-corona by taking a pixel-by-pixel minimum over a time interval of 56 days failed, and they recognized that their background model did contain some K-corona signal, thus confirming our above reservations about this technique. They then imposed an ad-hoc slope on their background model, adjusting it so as to minimize the K-corona contribution at the lower heights, and they derived an approximation of the F-corona. This highly empirical method strongly depends upon the specific image being analyzed and is not really adapted to the processing of long time series of images. It was later applied by Fainshtein (2007, 2009) to a few C2 images spanning Solar Cycle (hereafter abbreviated to SC) 23 assuming that the slope determined by Hayes, Vourlidas, and Howard (2001) holds throughout this cycle, and further extended it to C3 images using simple equatorial and polar profiles of the electron density to calculate the K-corona to be subtracted.

Two subsequent articles were devoted to this question, both making use of the method of Saito, Poland, and Munro (1977) implemented to investigate the equatorial and polar K- and F-coronal components on the basis of *Skylab* images obtained near the minimum of SC 20. Briefly, this method consists in inverting polarized brightness images pB to retrieve the electron density assuming a spherically symmetric spatial distribution, calculating the Thomson scattering, and subtracting the so-generated K-corona component to retrieve the F-component. Incidentally, a close variant of this method was proposed well before, namely by Von Klüber (1958), and also used in the *Skylab* context by Munro and Jackson (1977). Morgan and Habbal (2007) applied this method to four cases of LASCO-C2 images, two during the minimum and two during the maximum of SC 23 and produced equatorial and polar profiles that led them to reach conclusions about the stability of the visible F-corona. Dolei, Spadaro, and Ventura (2016) considered only one case in March 2008 during the SC 23/24 minimum and produced an intensity map of the F-corona highly distorted by the presence of a bright streamer on the eastern side, complemented by equatorial and polar profiles. In addition to the over-simplification of a spherical K-corona and the unproven accuracy of their photopolarimetric analysis, both articles ignored the question of the stray light and of the influence of the orbit of SOHO.

The first thorough analysis of the whole set of polarization sequences of LASCO-C2 images of 512×512 pixels obtained with the orange filter over 24 years [1996–2019] was performed by Lamy et al. (2020) who showed that extensive corrections are required to produce valid polarization and polarized radiance measurements. They concentrated on the production of complete sets of K-corona and pB images and inverted the latter images using a two-dimensional procedure developed by Quémerais and Lamy (2002) to produce maps of the electron density over 24 years [1996–2019]. They left open the question of separating the two unpolarized components, “F” and “SL” standing for F-corona and stray light, respectively (Figure 1), as well as that of retrieving the K-corona from the more numerous, routine high resolution images of 1024×1024 pixels. It is the purpose of the present article to tackle these two questions and thus complete the quantitative analysis of the whole set of LASCO-C2 images

obtained with the orange filter. It is organized as follows: We first discuss the constraints and obstacles facing the restoration of the F-corona. We then describe our elaborated procedure, which leads first to the restoration of the stray light and in turn to the restoration of the F-corona from the “F+SL” images produced by the polarimetric analysis. These results are finally employed to extract the K-corona from the routine high-resolution LASCO-C2 images, and we characterize its temporal evolution in comparison with an index and a proxy of solar activity. We conclude by emphasizing the importance of polarization observations for the accurate restoration of the K- and F-coronae beyond $\approx 2 R_{\odot}$ from images obtained with space coronagraphs.

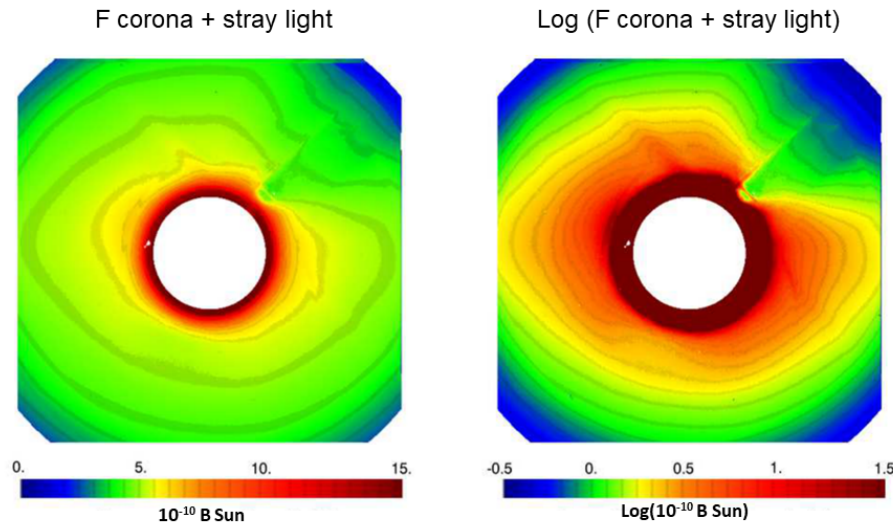


Figure 1. Two displays of an image resulting from the polarimetric analysis of Lamy et al. (2020) where the F-corona and the stray light are entangled. They have not been corrected for the vignetting effect to best reveal the different components of the stray light: the diffraction fringe surrounding the occulter (which extends to $2.2 R_{\odot}$), several arcs, and diffraction artifacts from the pylon. The left display uses a linear scale to best view the diffraction fringe. The right display uses a logarithmic scale to best view the distorted F-corona and the stray-light structures. For both displays, the units is $10^{-10} \overline{B_{\odot}}$.

2. Constraints and Obstacles Facing the Restoration of the F-corona

The photometrically accurate restoration of the F-corona from LASCO-C2 images is by no means a straightforward operation. We first summarize below the constraints and obstacles coming from the operations of SOHO and of LASCO, the difficulties inherent to the characterization of the F-corona, and the additional complications resulting from the presence of stray light, prominently the diffraction fringe surrounding the occulter.

2.1. Constraints from SOHO and LASCO Operations

SOHO was launched on 2 December 1995 and reached the L_1 Lagrangian point of the Sun–Earth system on 14 February 1996, where it was placed in a halo orbit with a period of 176.313 days. The orbit of SOHO, which is confined to the ecliptic plane, therefore results from a combination of an Earth synchronous elliptic orbit with a period of 365.249 days and this halo orbit whose period is very close to half of the main orbital period, i.e. its second harmonic. Consequently, the Sun–SOHO distance oscillates between typically 0.973 and 1.009 AU (≈ 209 and $217 R_\odot$) as illustrated in Figure 2.

The operation of SOHO experienced two major interruptions since 1996: first, an accidental loss of control during a roll maneuver on 25 June 1998, which resulted in a long data gap until recovery on 22 October 1998 and second a failure of the gyroscopes which caused another interruption from 21 December 1998 to 6 February 1999 when nominal operation resumed. On a short-term basis, there have been minor interruptions of a few days, typically two to three, which have no impact on the present work.

During its first year of operation, the attitude of SOHO was set such that its reference axis was aligned along the sky-projected direction of the solar rotational axis resulting in this direction being “vertical” (i.e. along the Y-axis of the CCD detector) with solar North up on the LASCO images. Starting on 10 July 2003 and following the failure of the motor steering its antenna, SOHO is periodically (every three months) rolled by 180° to maximize telemetry transmission to Earth. As seen on the LASCO images in the instrument reference frame, the sky-projected direction of the solar rotational axis remains “vertical” but solar North periodically alternates between up and down. This has severe consequences on the C2 images as the roll axis imposed by SOHO does not coincide with the C2 reference axis, which points to the center of the Sun: i) a periodic shift of the pixel coordinates of this center, and ii) a change of the stray-light pattern, further complicated by the intrinsic temporal evolution of the instrument performance. On 29 October 2010 and still on-going, the attitude of SOHO was changed to simplify operation: the reference orientation is fixed to the perpendicular to the ecliptic plane causing the projected direction of the solar rotational axis to oscillate between $\pm 7^\circ 15'$ around the “vertical” direction on the LASCO images. The temporal evolution of the roll angle of SOHO is presented in Figure 3.

The cadence of the “F+SL” images is by construction similar to that of the polarization sequences and is given in Figure 3 of Lamy et al. (2020), which displays the monthly averaged daily rate, one per day until 2008 inclusive and approximately four per day thereafter.

2.2. Constraints Associated with the Observation of the F-corona from 1 AU

Unlike the K-corona, which results from scattering of photospheric light by free electrons within a few ten or so solar radii, the F-corona predominantly results from diffraction by dust particles all along the line-of-sight, from the observer

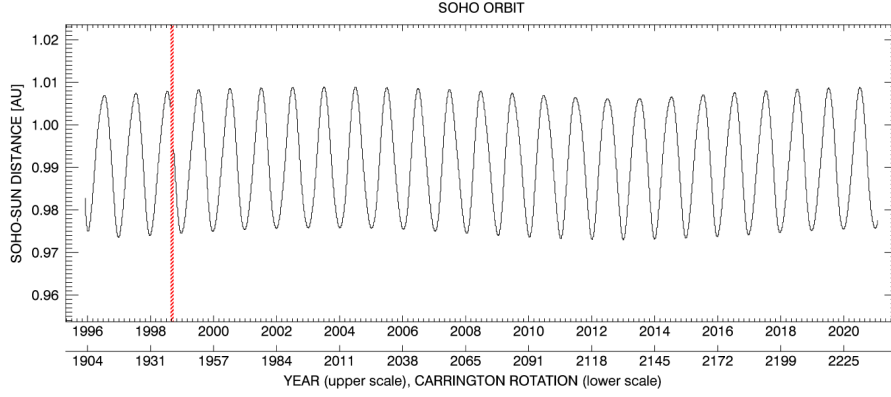


Figure 2. Temporal variation of the Sun–SOHO distance over 25 Years [1996–2020].

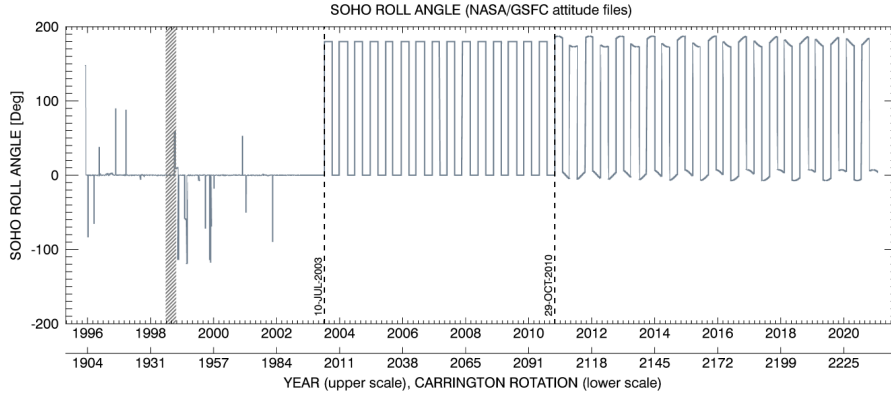


Figure 3. Temporal variation of the roll angle of SOHO over 25 Years [1996–2020].

to the circumsolar region and even beyond (Van de Hulst, 1947). As SOHO travels on its orbit which lies inside the zodiacal cloud, LASCO sees the F-corona from different vantage points with corresponding lines-of-sight sampling different regions of the cloud. Two main effects are therefore anticipated on the observed radiance of the F-corona: one resulting from the varying Sun–SOHO distance (3.6%) and the other from the oscillation of SOHO about the plane of symmetry of the inner zodiacal cloud (hereafter abbreviated “PSZC”), which is close to the solar equatorial plane according to Leinert and Grun (1990), whereas the orbit of SOHO lies in the ecliptic plane. This latter effect is expected to create an imbalance having its largest amplitude in the north and south directions. Conversely, the orbit of SOHO crosses the symmetry plane twice per year in late June and late December (at the so-called nodes) at which times the F-corona appears quasi-symmetric. It is interesting to note that the line of nodes is fortuitously closely aligned with the major axis of the elliptic orbit of SOHO so that the two variations are uncoupled to a large extent: the maximum effect

of the varying Sun–SOHO distance takes place very near the nodes whereas the maximum effect of the inclination of the symmetry plane is observed in quadrature. These two effects are amplified in Figure 4 to help in understanding how they affect the LASCO observations of the F-corona.

2.3. Problems Associated with the Stray Light

The polarimetric analysis of the LASCO-C2 images developed by Lamy et al. (2020) aimed at recovering the images of the polarized radiance pB of the K-corona, and in turn of the electron density. Henceforth, the processing included a correction for the instrumental vignetting so that the left-over unpolarized “F+SL” images of interest to the present work were corrected for this effect. This is obviously fine for the F-corona but not for the stray light, which is an internal instrumental effect seen by the unvignetted optical pupil of the coronagraph. Consequently, the stray light and particularly the diffraction fringe surrounding the occulter are artificially enhanced, thus appearing brighter than in reality (Figure 5). This constitutes a serious difficulty that the analysis aimed at restoring the F- and SL-components must cope with, further complicated by the fact that both vary with the Sun–SOHO distance differently, as we shall see.

3. Procedure of the Restoration of the F-corona

Our procedure of restoring the F-corona is quite complex and is composed of three main stages, each involving different steps. We first present an overview to help in understanding the flow of operations.

3.1. Overview of the Procedure

The analysis of the whole set of the LASCO-C2 polarization sequences by Lamy et al. (2020) performed the separation of the polarized K-corona and the unpolarized component “F+SL” composed of the F-corona and the instrumental stray light “SL”. Our procedure of restoring the F-corona makes use of the time series S_0 of these “F+SL” images, which extends over 24 years, from 1996 to 2019 inclusive. As emphasized by Lamy et al. (2020), the polarimetric technique implemented in the LASCO instrument and based on three identical linear polarizers with orientations at $+60^\circ$, 0° , and -60° is far from ideal and the separation is consequently not perfect. Careful inspection of the “F+SL” images indeed revealed the presence of traces or remnants of the K-corona, especially from its brightest structures. This constitutes a supplementary difficulty that the procedure must cope with. We present below the three main stages of the procedure schematically summarized in Figure 6.

In Stage 1, we perform a global analysis of the S_0 time series aimed at separately determining the variation of the F- and SL-components with the Sun–SOHO distance and scaling the images accordingly. We then generate a new shorter time series S_1 by taking the median image for each Carrington rotation, thus attenuating the contamination by K-corona remnants.

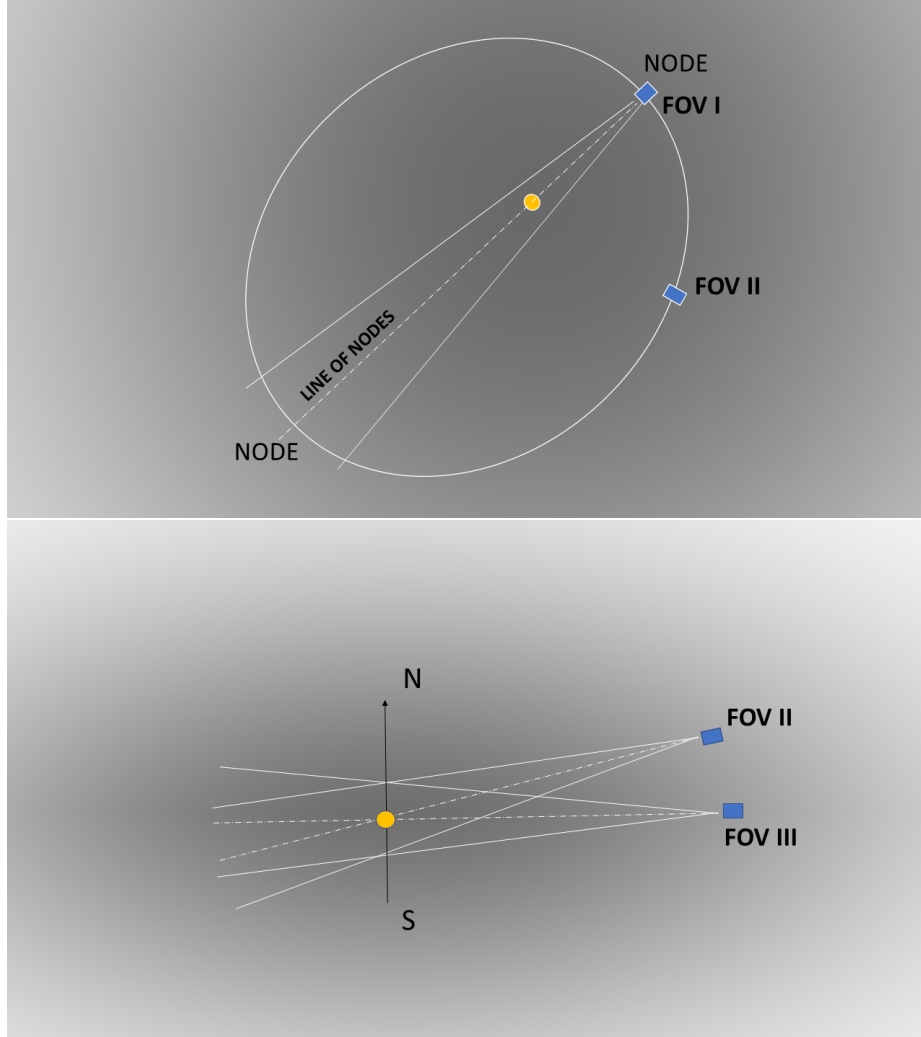


Figure 4. Schematic views of the geometry of LASCO observations of the F-corona from different vantage points immersed in the zodiacal cloud represented by the gray background. The upper panel shows the orbit of SOHO (white ellipse) in the zodiacal cloud as seen from above its plane of symmetry (PSZC). The line of nodes defined by the intersection of the orbital plane of SOHO (the Ecliptic plane) and the PSZC is nearly aligned with the major axis of the elliptic orbit. Its eccentricity is grossly amplified to highlight the difference of heliocentric distances at the two nodes, ≈ 0.973 and ≈ 1.009 AU. FOV I corresponds to an observation at one node whereas FOV II corresponds to an observation in quadrature when SOHO is near its extreme elevation from the plane of symmetry. This is best seen in the lower panel where this plane is seen edge-on. FOV III corresponds to FOV I of the upper panel, but artificially rotated by 90° to best highlight the different regions of the zodiacal cloud seen from the nodes and from the points in quadrature (i.e. along the minor axis of the elliptic orbit).

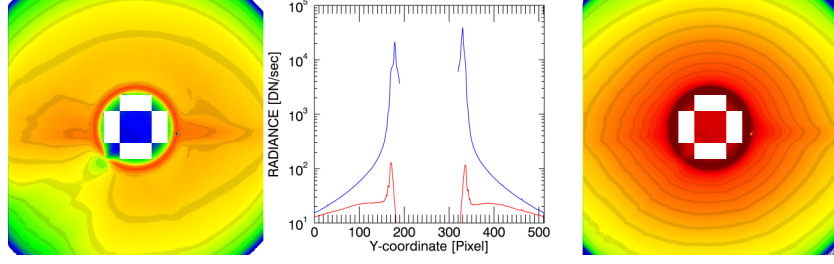


Figure 5. Illustration of the vignetting effect on the LASCO-C2 images. Left panel: a raw image of 512×512 pixels obtained on 9 January 1997. Right panel: the same image corrected for the vignetting effect. Central panel: radial profiles along the south–north direction of the raw image (red curve) and of the corrected image (blue curve). This illustrates the artificial enhancement of the diffraction fringe.

The main purpose of Stage 2 is the restoration of the stray light. In a first step, we construct mean images by applying a two-year sliding window with a time step of one year to the S_1 time series to force the F-corona to become artificially symmetric so as to facilitate the F–SL separation. This results in a new time series S_2 which is split into two time series $S_2(0)$ and $S_2(180)$ after 10 July 2003 according to the roll angle of SOHO. In a second step, we construct a parametric model of this symmetric F-corona. The third step is devoted to the final restoration of images of the stray light after defining time intervals during which they may be considered constant.

In Stage 3, we perform the restoration of the F-corona starting from a new time series S_3 which combines the $S_2(0)$ and $S_2(180)$ time series. A Fourier analysis in the temporal domain for each point of the corona (i, j) yields a set of images of the Fourier coefficients $C_F(\text{raw})$, which are subsequently filtered in the spatial domain. The resulting coefficients $C_F(\text{filter})$ are finally used to construct the final daily images of the F-corona, named “Fcor”, throughout the first 24 years of the mission [1996–2019].

Our procedure is reminiscent of that implemented by Stenborg and Howard (2017) for estimating (and removing) the background in STEREO HI-1 images in the sense that both rely on the different morphology and spatial frequencies of the components to be separated. However, we point out that their application to a LASCO-C2 image (their Figure 14) has nothing to do with this present work. Their “background”, which most likely includes the F-corona and the background (smooth) K-corona is used to construct the ratio with the original image. In essence, this is equivalent to an unsharp-masking operation aimed at revealing the K-corona structures and a CME at the expense of losing the photometry.

3.2. Stage 1: Global Analysis of the Time Series of “F+SL” Images

As already mentioned in Section 2, the temporal variation of the Sun–SOHO distance d affects the radiance of both the F-corona and the stray light. The F-corona increases as d decreases and we expect a power law variation $d^{-\nu_F}$ close

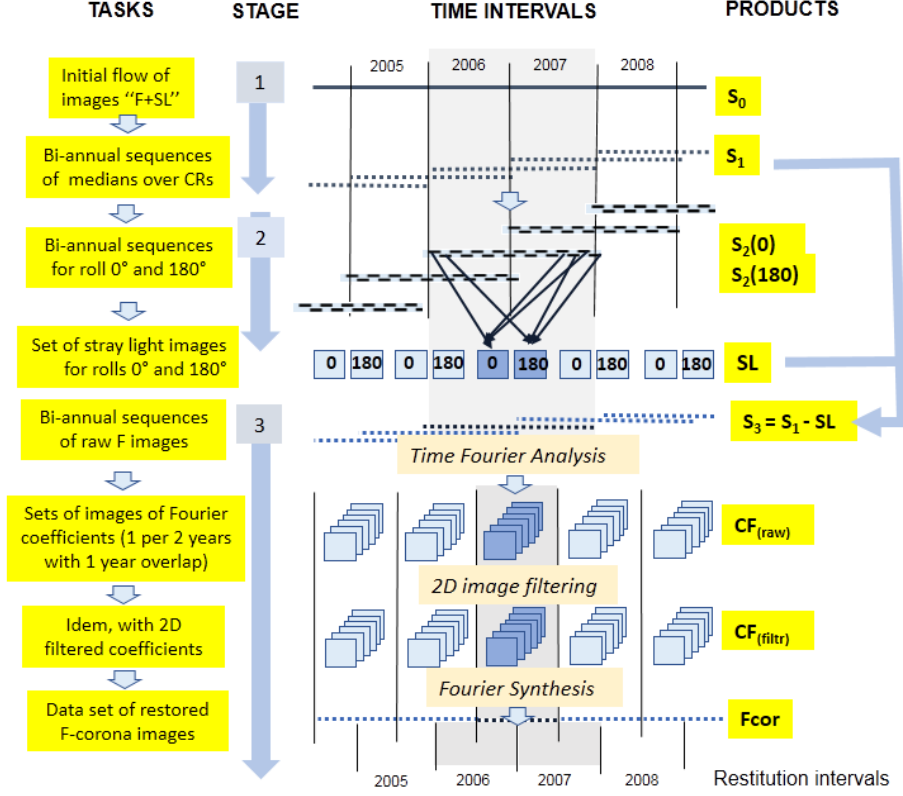


Figure 6. Schematic representation of the procedure aimed at separating the F- and SL-components from the "F+SL" images produced by the polarimetric analysis (S_0 time series). The upper part of the diagram corresponds to Stages 1 and 2 of the procedure aimed at recovering the stray-light images. The S_1 time series is obtained by taking the median image for each Carrington rotation. The S_2 time series results from the application of a two-year sliding window with a time step of one year split into two time series $S_2(0)$ and $S_2(180)$ according to the roll angle of SOHO; they are used to generate the images of the stray light. The lower part of the diagram corresponds to Stage 3 of the procedure aimed at the restoration of the F-corona. After subtracting the stray light, the $S_2(0)$ and $S_2(180)$ are combined in a common coronal reference time series S_3 and its Fourier analysis yields a set of images of the Fourier coefficients $C_F(raw)$. These images are filtered and the resulting coefficients $C_F(filter)$ are used to construct the final daily images "Fcor" of the F-corona.

to that found by the two *Helios* space probes $d^{-2.3 \pm 0.05}$ from measurements between 0.3 and 1 AU (Leinert et al., 1981). The stray light increases as well due to the change in the apparent size of the Sun, and we will see later that its variation $d^{-\nu_{SL}}$ is much steeper than that of the F-corona since it is prominently controlled by small-angle diffraction by the occulter.

In order to build an homogeneous time series of "F+SL" images, we must first determine these variations, that is the two power exponents ν_F and ν_{SL} , and normalize the images according to which component F or SL will be studied;

this is the aim of the first step of Stage 1. To do so, we define three circular regions or rings as illustrated in Figure 7.

- A narrow ring isolating the diffraction fringe defined by its inner and outer radii of 76.5 and 86 pixels, respectively.
- A broad intermediate ring extending radially from 86 to 200 pixels where the F-corona may still be affected by remnants of stray light and K-corona.
- A narrow outer ring extending radially from 200 to 250 pixels where the F-corona is presumed to be nearly free of any stray effects since the contributions from the stray light and the K-corona are expected to be vanishingly small.

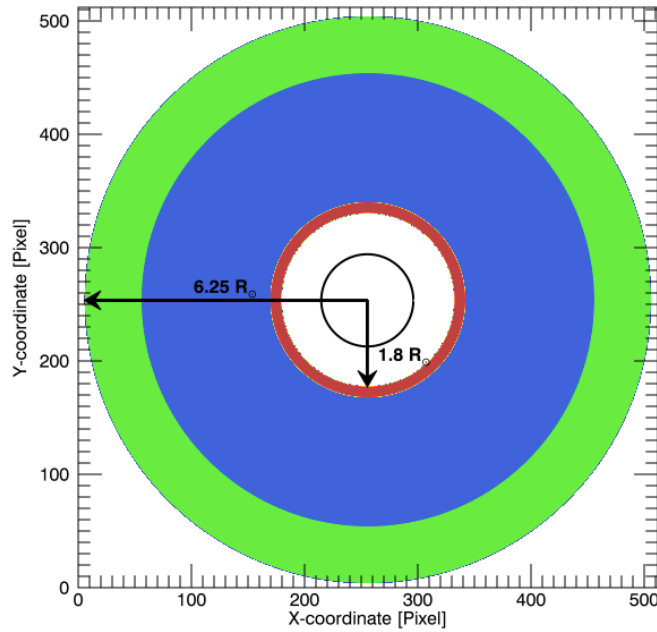


Figure 7. Illustration of the three concentric rings applied to the “F+SL” images of 512×512 pixels to study the photometric variation of the F-corona and the stray light with the Sun—SOHO distance. The black circle represents the solar disk. The red ring isolates the diffraction fringe. In the blue ring, the F-corona is affected by stray effects whereas in the green ring, these effects are presumed to be absent.

Integrating the radiances in these rings has the benefit of removing the periodic North–South asymmetry affecting the F-corona when SOHO moves back and forth about the symmetry plane of the zodiacal cloud, so that their temporal variations prominently reflect the effect of the varying Sun–SOHO distance. The integrations in the intermediate and outer rings are performed on the “F+SL”

images, since they properly record the F-corona, whereas that in the inner ring is performed on the vignetted “F+SL” images, since they correctly record the diffraction fringe as explained in Section 2.3. The temporal variations of the three integrated radiances are displayed in Figure 8, and their periodic oscillations are clearly in phase with the yearly variations of the Sun–SOHO distance. The long-term trend of the radiance of the fringe is remarkably stable with only slight variations. After the recovery of SOHO in 1998, it increased by 5 %, probably a consequence of a slight offset between the pre- and post-pointings. Thereafter, the radiance remained at a quasi-constant level until 2010 when the general level increased by 1.2 % and remained constant until 2015. The next three years witnessed a slight continuous decrease which leveled off during the following two years. Compared with the [1999–2010] time interval, the present general level is reduced by 2.4 %. The long-term trends of the radiance in the middle and outer rings follow similar evolutions: stable until 2006, then a progressive increase culminating in 2011 with a 5 % increase, followed by a decrease in 2016 and a turnover in 2019, all these fluctuations remaining at the level of a few percent. The influence of the K-corona residuals mentioned in Section 3.1 may be perceived by the irregularities in the amplitudes of the yearly variations during the two solar maxima and the simultaneous presence of high-frequency fluctuations best seen in the minima of the curves. In addition, the prominent peak present in the case of the middle ring at the end of 2014 reflects the anomalous surge that affected the K-corona as described by Lamy et al. (2017).

Figure 9 displays the three scatter plots corresponding to the three rings where the logarithm of the integrated radiance is plotted versus the logarithm of the Sun–SOHO distance. Whereas the fringe exhibits a clear linear trend allowing us to unambiguously derive a power exponent $\nu_{\text{SL}} = 5.672$, the behaviour of the two others is quite complex and an in-depth analysis revealed that it results from the superposition of the long-term temporal evolution and of the combination of the annual (SOHO’s orbit) and semi-annual (node crossings) variations. The second effect basically replaces the expected linear curve by a “Lissajous type” curve, whereas the first effect blurs the scatter plot. Disentangling these effects required an extra analysis starting with the determination and the subtraction of the long-term trends. This was achieved by either tracking the extrema of the temporal variations or applying a running average with a window of one year; the two approaches perform equally well. Then the separation of the annual and semi-annual variations was achieved by iteratively fitting a power-law of the Sun–SOHO distance to the temporal variations. This quickly converged and resulted in power-law variations as illustrated by the case of the outer ring displayed in the lower-right panel of Figure 9. This procedure yielded robust determinations of the power exponents: 2.154 for the outer ring and 2.926 for the middle one.

An alternative procedure was applied consisting in considering only the radiance values at the nodes, exploiting the fact that they take place at nearly the extreme values of the Sun–SOHO distance as pointed out in Section 2. The nodes further offer an advantage as C2 sees the *same* volume of the zodiacal cloud from two opposite vantage points so that the variation of the radiance between consecutive nodes can be safely attributed to the varying Sun–SOHO distance. This approach bypasses the tasks of determining the long-term trend

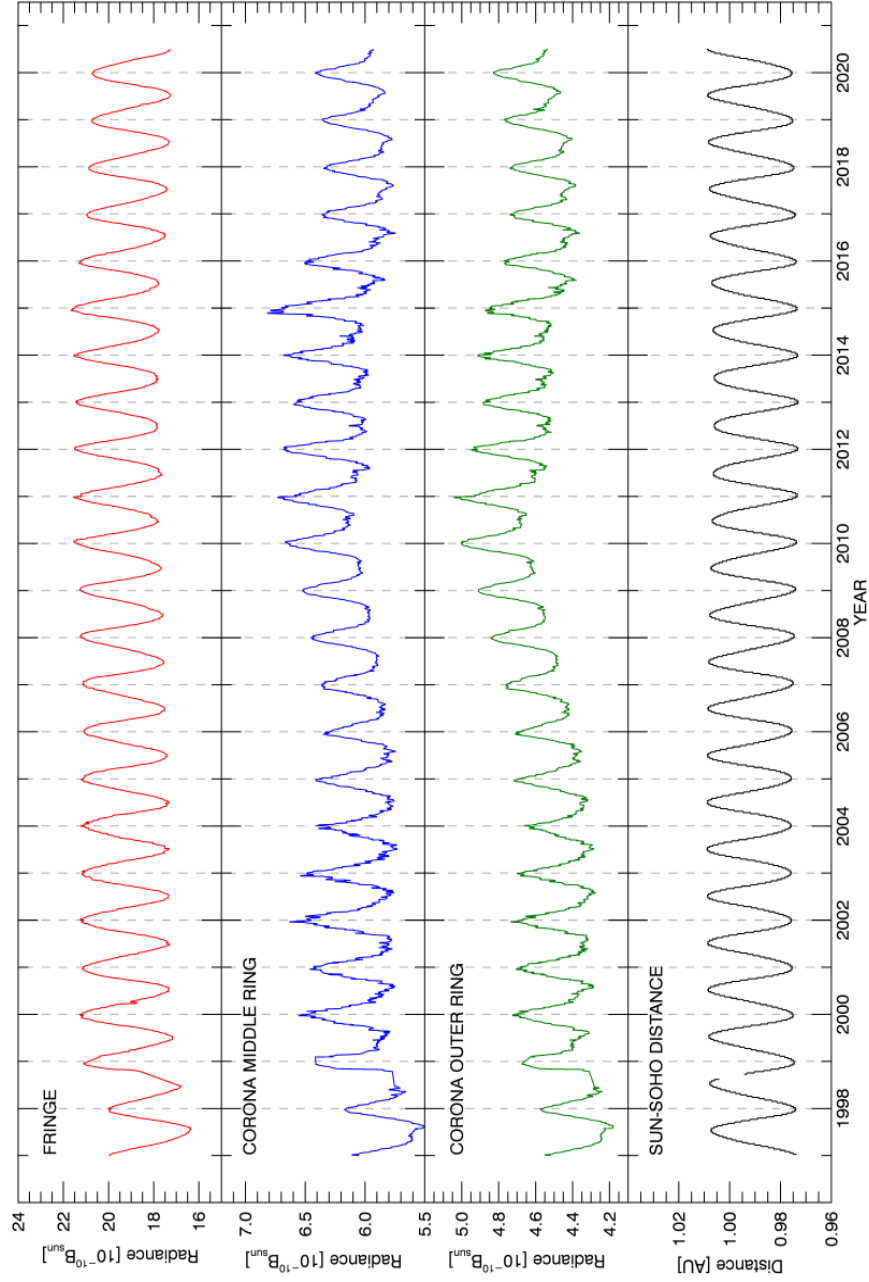


Figure 8. Temporal variation of the radiances of the “F+SL” images integrated in the three rings defined in Figure 7 over 24 years (upper three panels). The colors correspond to the rings depicted in Figure 7. The lower panel displays the variation of the Sun–SOHO distance.

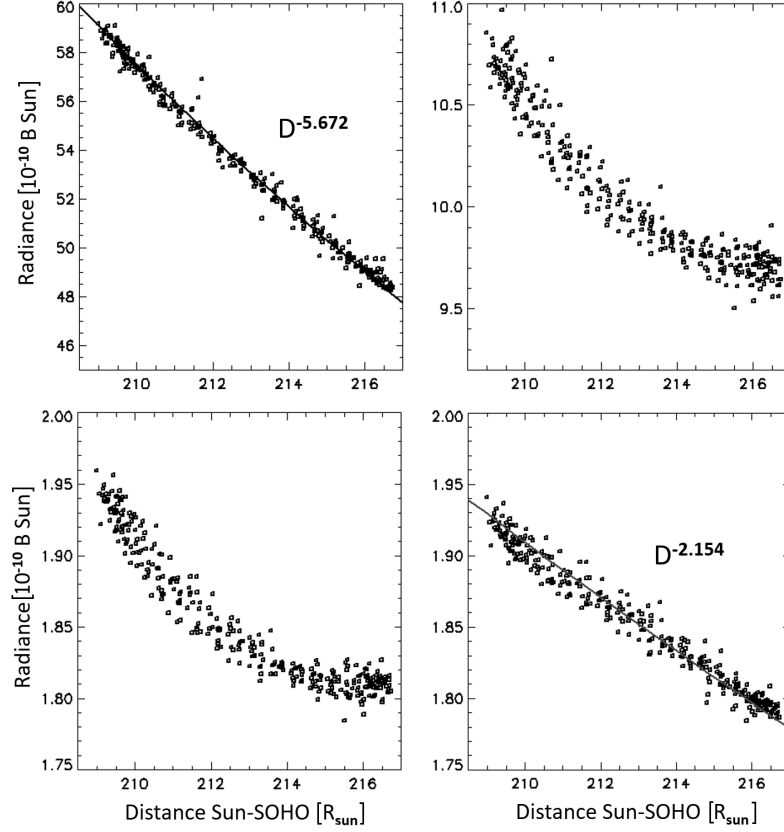


Figure 9. Scatter plots of the integrated radiance in the three rings versus the Sun-SOHO distance on a log-log scale: inner fringe ring (upper-left panel), middle ring (upper-right panel), and outer ring (lower-left panel). The lower-right panel displays the effect of de-trending the radiance in the outer ring by removing the semi-annual variation.

and of disentangling the annual and semi-annual variations. Individual power exponent values were thus derived every half-year and averaging them produced global values over 24 years. Figure 10 illustrates this determination for the outer ring yielding a power-law exponent of 2.132 to be favorably compared with 2.154 from the first method. It is interesting to note that, except for the first years when the accidental interruptions of SOHO may have introduced a bias, the largest fluctuations are recorded during the maxima of SC 23 and 24, possibly suggesting some influence of the K-corona at those times even in the outer ring. Removing these spurious data points reduces the power exponent to 2.058, which is probably a more realistic value for the F-corona. The standard deviation appears quite large, 0.31 in the nominal case and 0.19 after removing the “outliers”, underlying the sensitivity of the power exponent to the data.

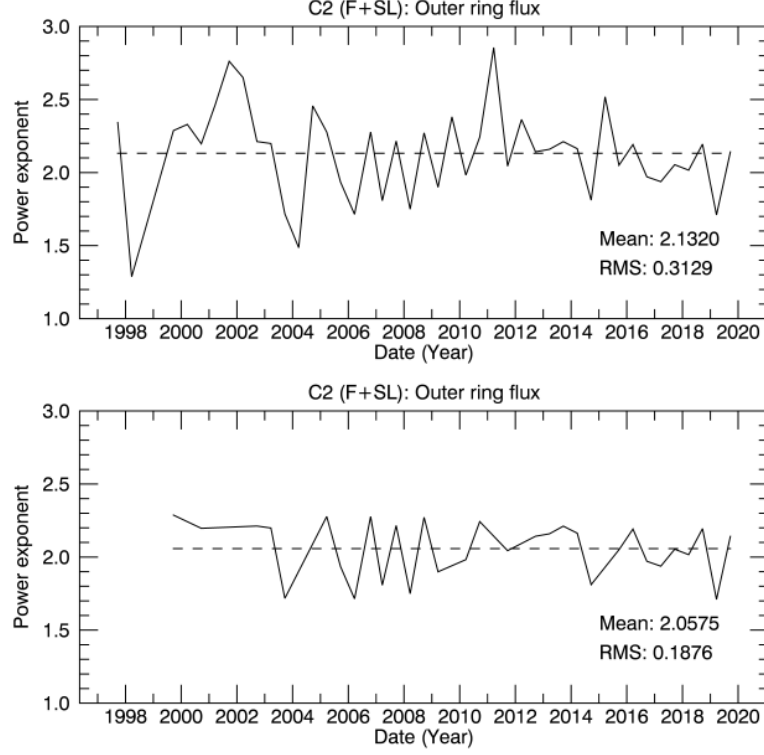


Figure 10. Temporal evolution of the power exponent ν_F of the variation of the radiance of the “F+SL” images integrated in the outer ring. The upper panel displays the complete data set and the lower one excludes the largest fluctuations, see text for detail.

Let us come back to the large difference between the values of the power exponent found for the middle and outer rings. This was investigated by subdividing the middle ring into four sub-rings of approximately the same width, and we did find a progressive reduction of the exponent from 3.685 in the innermost sub-ring to the value mentioned above in the outer ring. There is little doubt that we are witnessing the diminishing influence of the stray light with increasing solar elongation, starting from an exponent of 5.672 for the fringe itself. This complicated the adoption of a single power-law variation for the F-corona in the “F+SL” images, and we made a compromise by retaining an average value $\nu_F = 2.3$ as obtained in the sub-ring located half-way in the C2 field of view.

The final step of Stage 1 consisted in correcting the “F+SL” images for the varying Sun–SOHO distance (according to the function $d^{-\nu_F}$) and reducing their large number by taking the median images calculated for each Carrington rotation. This procedure produced a time series of 312 images called S_1 and offered the additional benefit of mitigating the effects of the K-corona residuals.

3.3. Stage 2: restoration of the Stray Light

Due to the stability of both the pointing of SOHO and the C2 instrument, we expect the stray light to be stable certainly not over the whole mission, but on time-scales much larger than a Carrington rotation so that the sampling of the S_1 time series is not relevant and necessary for its restoration. Another aspect comes into play as the F-corona must be regularized or smoothed as much as possible to facilitate the F/SL separation.

The first step of Stage 2 consisted in generating a new reduced time series S_2 satisfying the above prescriptions, and this was achieved by constructing mean images using a two-year sliding window with a time step of one year. Each image denoted $I_M(i, j)$ with $i, j = \{1 \dots 512\}$ is therefore the mean of 26 images of the S_1 time series. This process removes the yearly variation of the F-corona and creates a symmetric “mean F-corona” superimposed on a mean stray light. This “mean F-corona” has no physical reality but very much helps for the F/SL separation.

Starting on 10 July 2003, the quarterly SOHO rolls imposed the division of S_2 into two separate sub-series $S_2(0)$ and $S_2(180)$, which were processed independently. Indeed, preliminary investigations revealed a systematic change of the location of the center of the Sun between the two roll cases (the SOHO roll axis is evidently not strictly aligned with the C2 pointing axis) and slight changes of the stray-light pattern. In order to ensure a good continuity between successive years, the pre-roll 26 images were recovered by implementing the two-year window with an overlap of one year, which smooths the transition.

At this point, we had to consider the question of the stability of the stray light, that is to define time intervals during which it can be considered constant, and separately for the two roll cases. This was achieved by visual inspection of running differences between successive images of the $S_2(0)$ and $S_2(180)$ time series. Therefore, at the end of this first step, we obtained: i) a set of images $I_M(i, j)$ where a symmetric “mean F-corona” and an enhanced (by the vignetting correction) stray light are superimposed, and ii) a set of time intervals during which the stray light may be considered constant (Table 1). Note that any K-corona residuals are expected to be further reduced as a consequence of the double averaging resulting from the constructions of the S_1 and S_2 time series.

Table 1.: Start times in both Modified Julian Date (MJD) and calendar date of the intervals of validity of the different stray-light images for the years 1996 to 2019.

MJD	Calendar date	File name
50126.588	1996-02-13 14:06	SL_1996_1998_000
51099.000	1998-10-13 00:00	SL_1999_2000_000
51879.003	2000-12-01 00:00	SL_2001_2002_000
52312.764	2002-02-07 18:20	SL_2002_2003_000

52828.542	2003-07-08 13:00	SL_2003_2004_180
52919.465	2003-10-07 11:10	SL_2003_2004_000
53003.817	2003-12-30 19:36	SL_2003_2004_180
53094.775	2004-03-30 18:36	SL_2003_2004_000
53180.612	2004-06-24 14:41	SL_2004_2005_180
53270.956	2004-09-22 22:56	SL_2004_2005_000
53362.891	2004-12-23 21:23	SL_2004_2005_180
53452.879	2005-03-23 21:05	SL_2004_2005_000
53539.762	2005-06-18 18:17	SL_2005_2006_180
53622.515	2005-09-09 12:21	SL_2005_2006_000
53720.937	2005-12-16 22:29	SL_2005_2006_180
53808.171	2006-03-14 04:06	SL_2005_2006_000
53893.673	2006-06-07 16:09	SL_2006_2007_180
53989.743	2006-09-11 17:49	SL_2006_2007_000
54075.842	2006-12-06 20:12	SL_2006_2007_180
54164.996	2007-03-05 23:54	SL_2006_2007_000
54251.062	2007-05-31 01:29	SL_2007_2008_180
54344.075	2007-09-01 01:48	SL_2007_2008_000
54425.117	2007-11-21 02:48	SL_2007_2008_180
54519.884	2008-02-23 21:12	SL_2007_2008_000
54607.032	2008-05-21 00:46	SL_2008_2009_180
54700.695	2008-08-22 16:40	SL_2008_2009_000
54790.397	2008-11-20 09:31	SL_2008_2009_180
54877.754	2009-02-15 18:05	SL_2008_2009_000
54963.886	2009-05-12 21:15	SL_2009_2010_180
55056.886	2009-08-13 21:15	SL_2009_2010_000
55144.618	2009-11-09 14:49	SL_2009_2010_180
55231.879	2010-02-04 21:05	SL_2009_2010_000
55316.942	2010-04-30 22:36	SL_2010_2011_180
55410.811	2010-08-02 19:27	SL_2010_2011_000
55498.939	2010-10-29 22:32	SL_2010_2011_180
55586.642	2011-01-25 15:24	SL_2010_2011_000
55673.755	2011-04-22 18:07	SL_2011_2012_180
55764.833	2011-07-22 19:59	SL_2011_2012_000
55854.971	2011-10-20 23:18	SL_2011_2012_180
55944.300	2012-01-18 07:12	SL_2011_2012_000
56028.940	2012-04-11 22:33	SL_2011_2012_180
56032.342	2012-04-15 08:12	SL_2012_2013_180
56120.947	2012-07-12 22:43	SL_2012_2013_000
56210.018	2012-10-10 00:25	SL_2012_2013_180
56299.841	2013-01-07 20:11	SL_2012_2013_000
56400.684	2013-04-18 16:24	SL_2012_2013_180
56410.084	2013-04-28 02:00	SL_2013_2014_180
56476.742	2013-07-03 17:48	SL_2013_2014_000
56565.917	2013-09-30 22:00	SL_2013_2014_180
56663.919	2014-01-06 22:03	SL_2013_2014_000

56770.659	2014-04-23 15:48	SL_2013_2014_180
56831.882	2014-06-23 21:10	SL_2014_2015_000
56922.910	2014-09-22 21:50	SL_2014_2015_180
57015.709	2014-12-24 17:00	SL_2014_2015_000
57164.179	2015-05-22 04:17	SL_2014_2015_180
57185.855	2015-06-12 20:31	SL_2015_2016_000
57276.992	2015-09-11 23:48	SL_2015_2016_180
57366.876	2015-12-10 21:01	SL_2015_2016_000
57452.004	2016-03-05 00:05	SL_2015_2016_180
57542.903	2016-06-03 21:40	SL_2016_2017_000
57632.868	2016-09-01 20:49	SL_2016_2017_180
57721.788	2016-11-29 18:55	SL_2016_2017_000
57807.840	2017-02-23 20:09	SL_2016_2017_180
57897.788	2017-05-24 18:55	SL_2017_2018_000
57987.863	2017-08-22 20:42	SL_2017_2018_180
58077.754	2017-11-20 18:06	SL_2017_2018_000
58163.826	2018-02-14 19:50	SL_2017_2018_180
58253.822	2018-05-15 19:44	SL_2018_2019_000
58343.723	2018-08-13 17:21	SL_2018_2019_180
58436.747	2018-11-14 17:56	SL_2018_2019_000
58519.826	2019-02-05 19:50	SL_2018_2019_180
58610.691	2019-05-07 16:35	SL_2018_2019_000
58582.191	2019-08-04 16:35	SL_2018_2019_180
58792.749	2019-11-05 17:59	SL_2018_2019_000
58877.856	2020-01-29 20:32	SL_2018_2019_180

The second step of Stage 2 consisted in constructing a model of the “mean F-corona” exploiting its properties of symmetry with respect to the x- (east–west) and y- (south–north) axes and the fact that the stray-light pattern is prominently dominated by the narrow diffraction fringe with a faint extension up to ≈ 160 pixels from the center, thus leaving the outer part nearly free of parasitic light. The procedure started by taking the logarithm of the radiance of the $I_M(i, j)$ images and transforming them in polar coordinates (ρ, θ) whose origin is at the center of symmetry of the “mean F-corona”. This center was defined by cross-correlating the direct and reversed radial profiles along the x- and y-axes, excluding the inner zone where the stray light dominates. Circular profiles were extracted from each polar transformed images at constant radii ρ_k and fitted with polynomials of degree six retaining only the even exponents:

$$P(\theta, \rho_k) = a_0(\rho_k) + a_2(\rho_k)\theta^2 + a_4(\rho_k)\theta^4 + a_6(\rho_k)\theta^6 .east$$

The assumed symmetry of the “mean F-corona” allowed us restricting the fits to half profiles, from one maximum (east side) to the other (west side), and we

avored the northern hemisphere to avoid the sector contaminated by stray effects associated with the pylon. Additional constraints were introduced in the fitting process, notably the continuity at the maxima (first derivatives equal to zero) and the positivity of the residuals “raw profiles minus fitted profiles”. This latter conditions in fact imposed that the fitted profiles are lower envelopes of the raw profiles (Figure 11). The variations of the coefficients $a_{2i}(\rho_k)$ with $i = 0, 1, 2, 3$ as functions of ρ_k were analyzed and all displayed a clear transition from the regime of the F-corona to that of the diffraction fringe, so that the former regime could be extrapolated inward to recover the corrected “mean F-corona” down to the inner limit of the field of view. These extrapolated coefficients were used to construct new polar images $P(\theta, \rho)$, which were then transformed back to Cartesian images yielding the corrected “mean F-corona” $F_0(i, j)$. A formal and detailed description of this procedure is given by Llebaria, Loirat, and Lamy (2012).

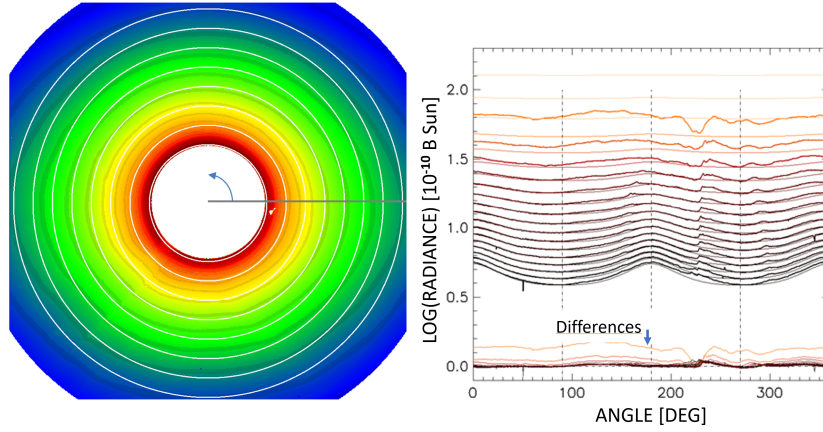


Figure 11. Image of a “mean F-corona” with a subset of overlaid white circles (left panel) used to extract the polar profiles shown in the right panel. The polar development starts from the horizontal right radius (black line on the image) and proceeds counterclockwise. The raw profiles are represented by thick lines and the restored ones using the polynomial fitting procedure by thin lines. Differences between the logarithm of the two corresponding profiles are displayed below in the 0.0 to 0.3 range.

The third and final step of Stage 2 consisted in generating the set of stray-light images by subtracting the $F_0(i, j)$ images from the $I_M(i, j)$ images, and removing the effect of the vignetting correction $\mathcal{V}(i, j)$ as explained in Section 3.2:

$$SL(i, j) = [I_M(i, j) - F_0(i, j)] \times \mathcal{V}(i, j).$$

Altogether, we produced a set of 36 stray-light images covering 24 years of LASCO-C2 operation from 1996 to 2019 inclusive. They are displayed in Figures 12, 13, and 14, each one including twelve images. Table 1 lists the dates of change of stray light, in other terms, the time intervals of the validity of each image. Note the systematic changes at each new roll maneuver.

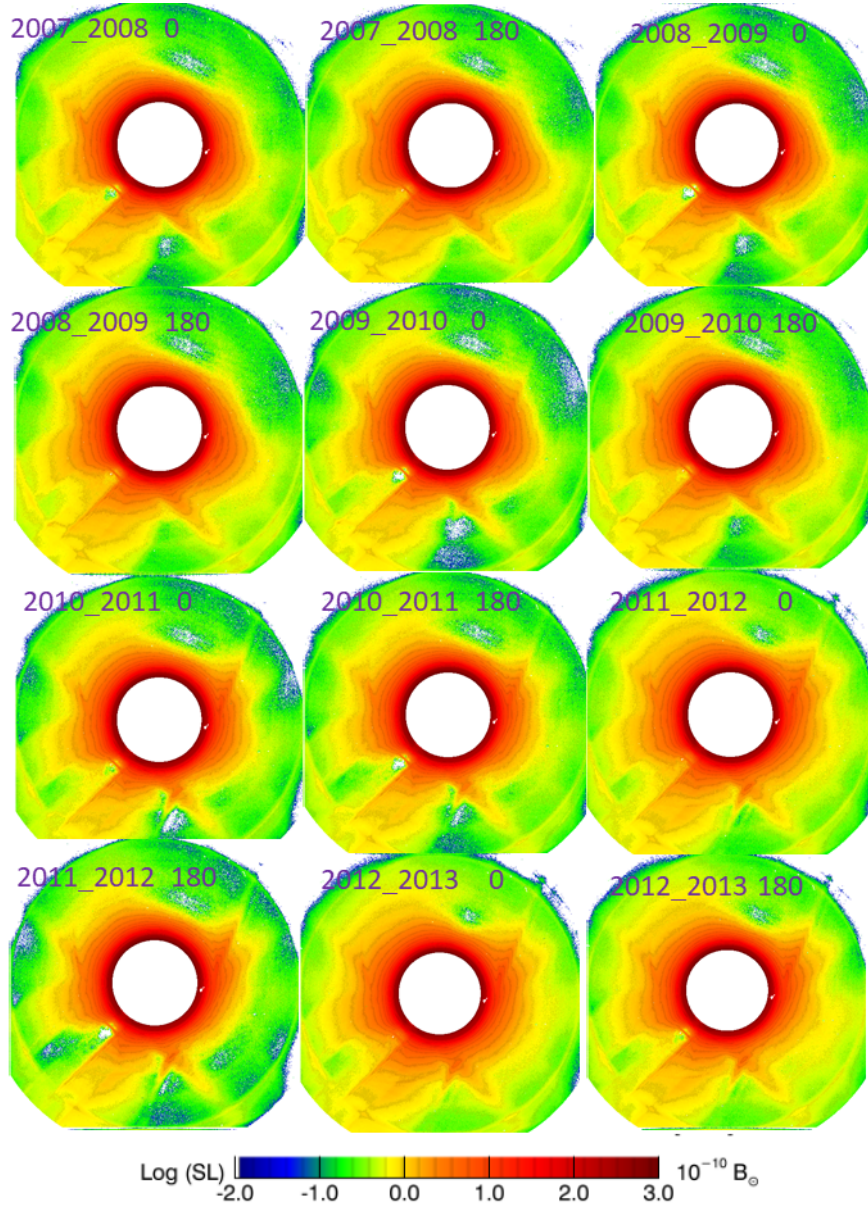


Figure 12. Images of the LASCO-C2 stray light over the time interval 1996 to 2007.

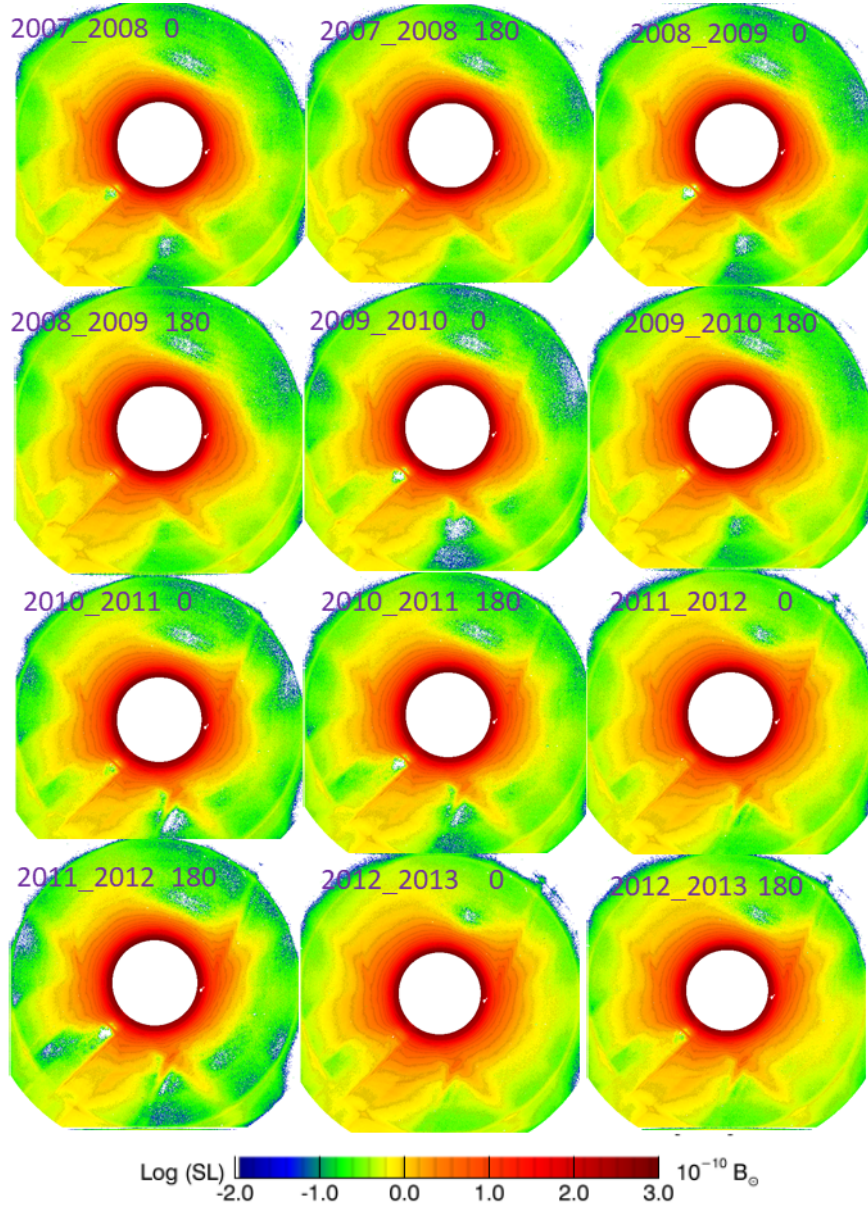


Figure 13. Images of the LASCO-C2 stray light over the time interval 2007 to 2013.

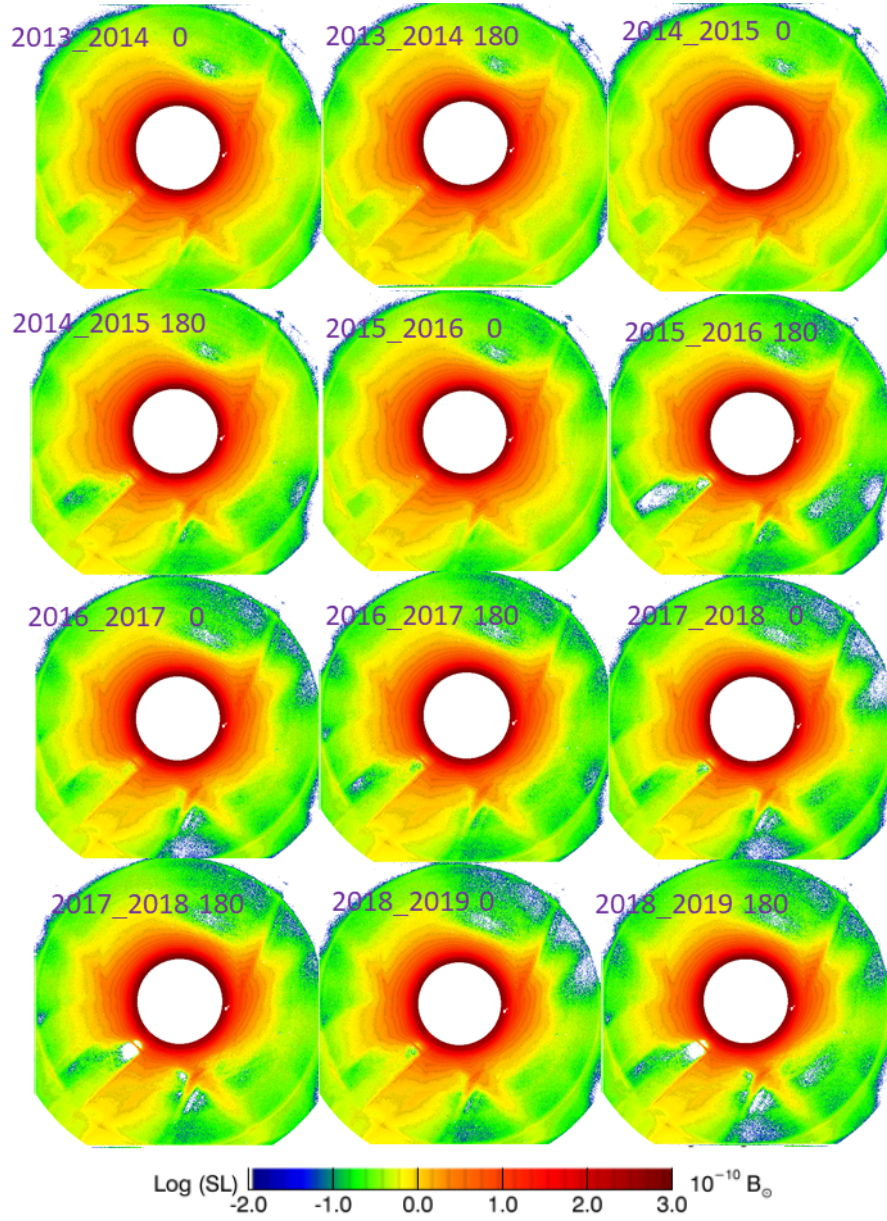


Figure 14. Images of the LASCO-C2 stray light over the time interval 2013 to 2019.

The photometric properties of the stray light are illustrated by radial profiles extracted along the east–west and south–north directions during the [2004–2018] time interval. The two cases of roll angles are displayed separately: 0° in Figure 15 and 180° in Figure 16. The profiles were taken at the same time of each year of the [2004–2018] time interval and piled up using different colors. The “F” profiles are indistinguishable, as their temporal variations from year to year amount to at most a few percent. The “SL” profiles exhibit substantial variability, but they tend to form sub-groups indicating the persistence of similar levels over several years and even of similar patterns, which implies that they are not noise. These profiles rapidly decrease with increasing radial distance from the center so that, at the edge of the square field of view of LASCO-C2, it levels off at approximately $10^{-11} \overline{B}_\odot$, that is a factor of ≈ 100 below the radiance of the F-corona in the equatorial direction and a factor of ≈ 60 in the polar direction, a quite remarkable achievement.

The two-dimensional patterns of the stray light may be grossly characterized by several components: the narrow bright diffraction fringe, its associated broad wings extending to approximately two third of the field of view, and different localized structures, some permanent like the radial reinforcement connected to one side of the pylon, some intermittent. The most important changes that occurred during the 24 years are highlighted in Figure 17. During the first years of operation, and until the accidental loss of SOHO in June 1998, the stray light remained constant and apart from the general pattern described above, exhibits two distinct streaks forming a V-shape, both being nearly tangent to the diffraction fringe. The one oriented at 45° (counterclockwise from the vertical direction) and labeled “S1” appears connected to the junction between the occulter and the pylon, although this may be fortuitous. The other one oriented vertically and labeled “S2” has no apparent origin. Following the re-pointing of SOHO in early 1999, a slight increase of the overall level of stray light is revealed by our analysis but went unnoticed at that time. In any case, as the diffraction fringe remained symmetric, a decision was made not to activate the mechanism controlling the centering of the inner occulter. Streak “S1” persisted, although becoming fuzzier, whereas “S2” completely disappeared in February 2002 and was later replaced by a new streak labeled “S3” at a different orientation ($\approx 30^\circ$ from the vertical direction) and also tangent to the fringe, thus forming a new V-shape with “S1”. “S3” can be traced to the 2009–2010 image, but it became conspicuous thereafter, persisting until 2019. It is worth emphasizing at this stage that none of the components of the stray light patterns, in particular the streaks, can be attributed to residuals of the K-corona, implying that our procedure has been fully successful in eliminating any such traces.

The general background level of stray light was quantified by integrating its radiance in a ring that excludes the diffraction fringe. This ring encompasses the middle and outer rings introduced in Section 3.2, and thus extends radially from 86 to 250 pixels. Figure 18 displays its temporal variation in the case of the roll angle of 0° since it extends over the whole interval of 24 years. It clearly reveals a correlation with solar activity with a modulation of $\approx 13\%$, which implies that a small component of the stray light has its origin in scattered light from the innermost bright corona.

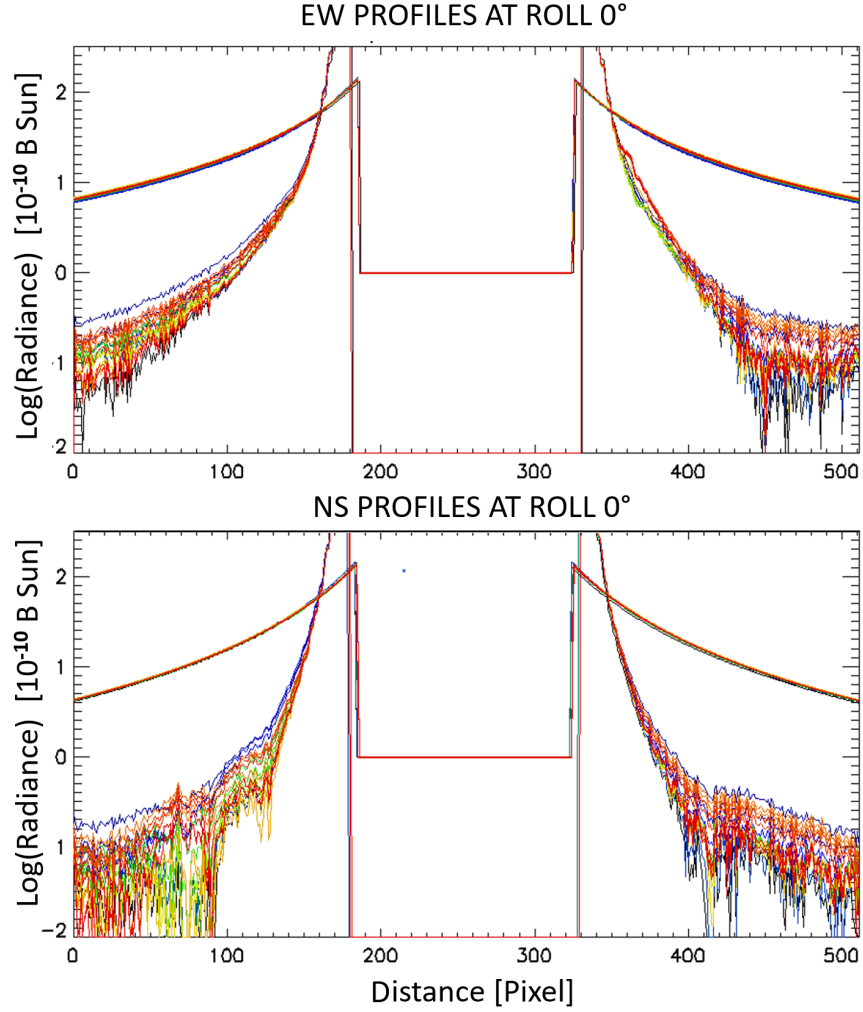


Figure 15. East–west (upper panel) and south–north (lower panel) radial profiles of the stray light (lower set of curves) and of the F-corona (upper set of indistinguishable curves) over the [2004–2018] time interval in the case of the SOHO roll angle of 0° .

3.4. Stage 3: restoration of the F-Corona

With the stray-light images in hand, we proceeded to restore the F-corona from the “F+SL” set of images by subtracting from each one the appropriate “SL” image. As part of the final step of Stage 1, the “F+SL” images were corrected for the varying Sun–SOHO distance according to the function $d^{-\nu_F}$. This is irrelevant for the “SL” images, which were thus corrected using the function $d^{(\nu_F - \nu_{SL})}$ in order to restore their correct variation with d . This procedure

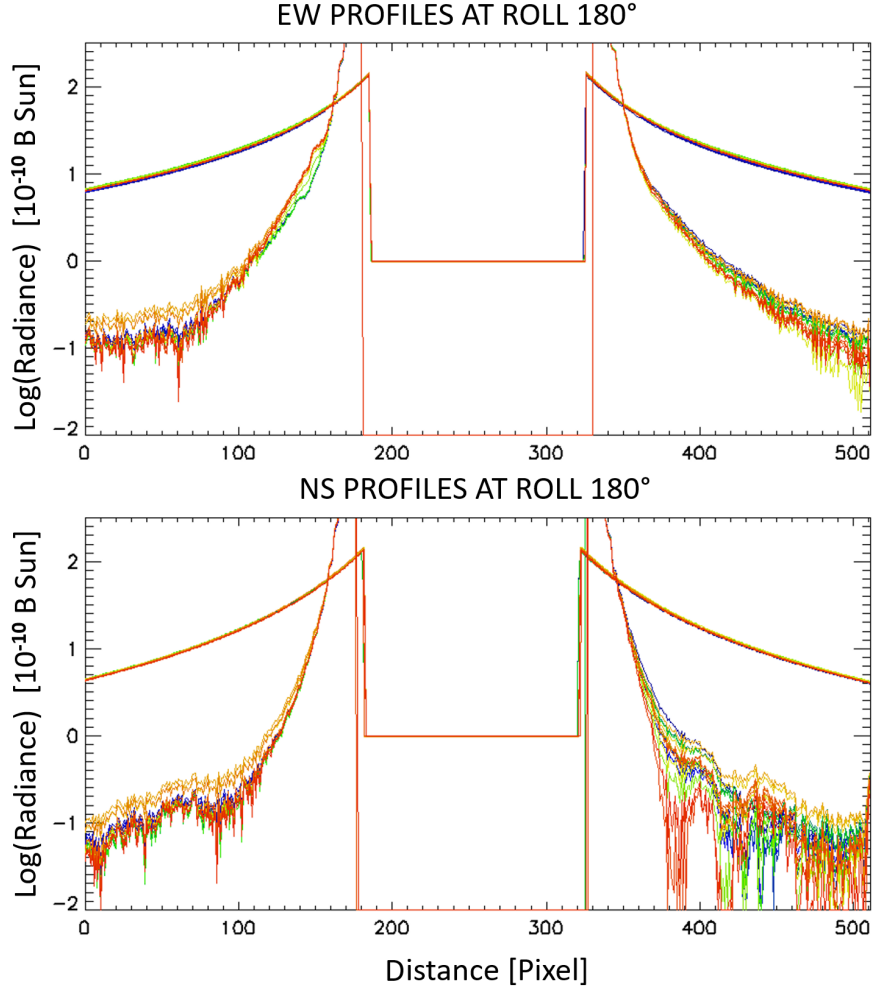


Figure 16. East–west (upper panel) and south–north (lower panel) radial profiles of the stray light (lower set of curves) and of the F-corona (upper set of indistinguishable curves) over the [2004–2018] time interval in the case of the SOHO roll angle of 180° .

yielded a first time series of “F” images labeled S_3 . They are still modulated by the annual oscillation of SOHO around the symmetry plane of the zodiacal cloud, and this effect can be fitted point-by-point by a Fourier series as described below.

We proceeded by structuring this S_3 series in blocks of two-year duration with an overlap of one year. Each pixel of the coronal field was tracked along a given two-year interval, and each temporal profile was subjected to a Fourier analysis limited to the third harmonics. This process led to the compression of

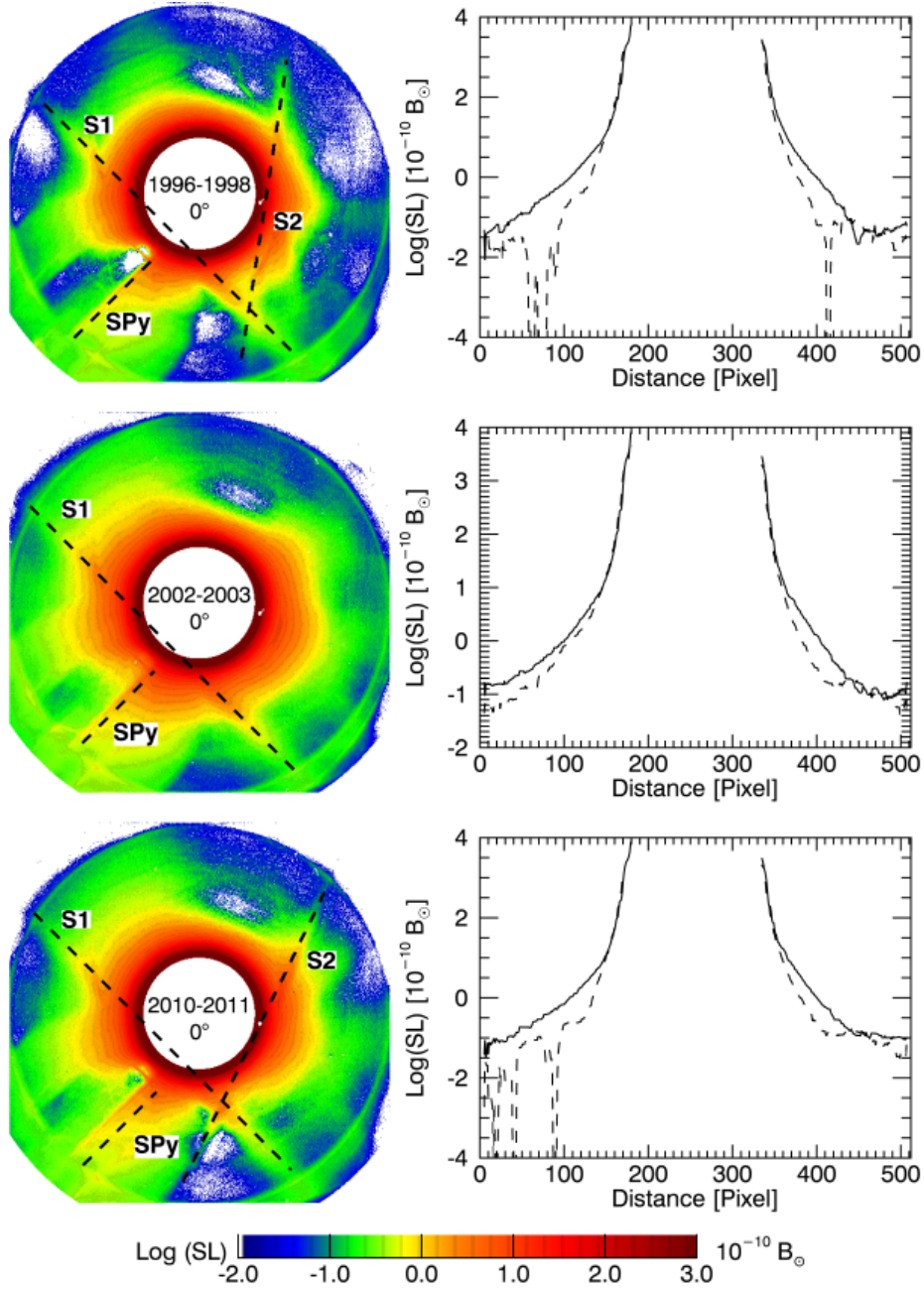


Figure 17. Illustration of the main changes in the stray-light pattern of LASCO-C2 (left column) and radial profiles along the east-west (solid lines) and south-north (dashed lines) directions extracted from the images (right column). These profiles were smoothed using a boxcar width of seven pixels for better legibility. Whereas the S1 streak and the stray-light feature SPy connected to the pylon persisted throughout the mission, the S2 streak present at the beginning of the mission disappeared in February 2002. The S3 streak appeared in 2010 and persisted thereafter.

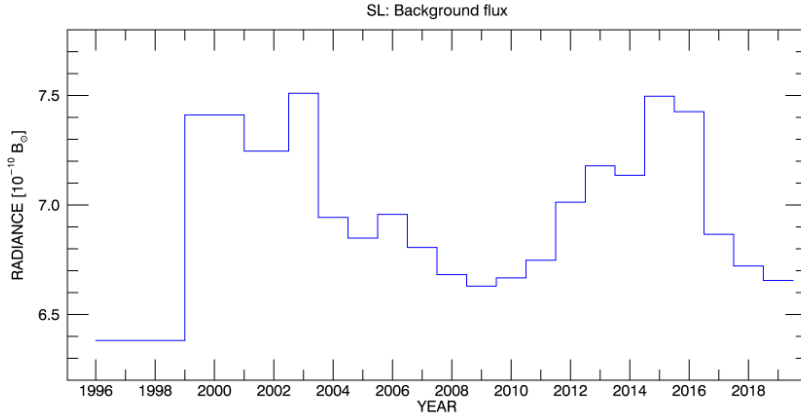


Figure 18. Temporal variation of the background radiance of the stray-light images at roll angle of 0° integrated in the outer ring defined in the text and in Figure 7. The temporal extent of each bin corresponds to the time interval of validity of the respective images.

the set of “F” images extending over a time interval of two years to a set of seven images: that of the mean value of the Fourier decomposition and those of the sine and cosine coefficient of the three harmonics. As the harmonics’ order increases, the images of the coefficients (ICs) become more and more sensitive to the local pixel-to-pixel noise in the “F” images. A bi-dimensional filtering was therefore applied to the six ICs after dividing them by the mean image to compensate for the strong radial gradient of the F-corona. After filtering, each IC was individually restored by multiplying each filtered IC with the mean image. Ultimately, seven coefficients were used to fit the annual evolution of the F-corona: one for the mean, and 3×2 for the three harmonics. Figure 19 displays an example such a set of seven images before and after filtering.

In order to mitigate the effect of the transition between the successive two-year time intervals, the validity of each set of Fourier coefficients was limited to a time interval of one year centered on each two-year interval, i.e. from 1 July of the first year to 30 June of the second one. The restoration of the final images of the F-corona was performed on a daily basis forming the “Fcor” time series. These images are in the format of 1024×1024 pixels, and their absolute radiance expressed in units of $10^{-10} \overline{B_\odot}$ is given at the heliocentric distance of SOHO at the specified date, both reported in the image header. Their orientations are such that North is always up. The vertical direction is aligned with the sky projected direction of the solar axis until 29 October 2010, and with the direction of the ecliptic (North) pole thereafter. Examples are given in Figure 20 corresponding to two views, at the June and December nodes of 1997, when the Sun–SOHO distance was nearly maximum and minimum, respectively.

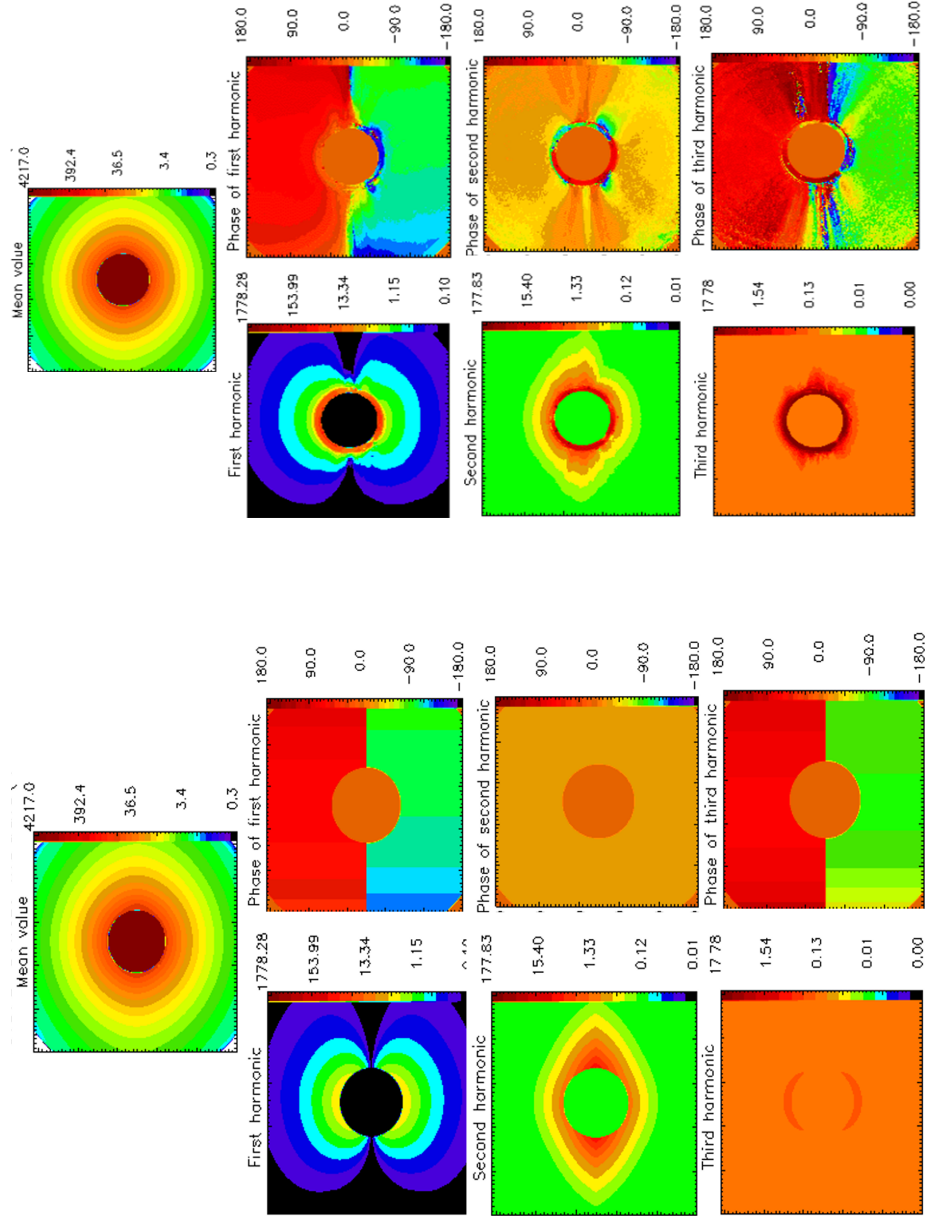


Figure 19. Illustration of the Fourier analysis of a time series of “F” images (left block of images) and of the effect of filtering the coefficients (right block of images). In each block, the upper single image corresponds to the mean value. Below, the modulus (left column) and phase (right column) of the coefficients are displayed for the first three harmonics.

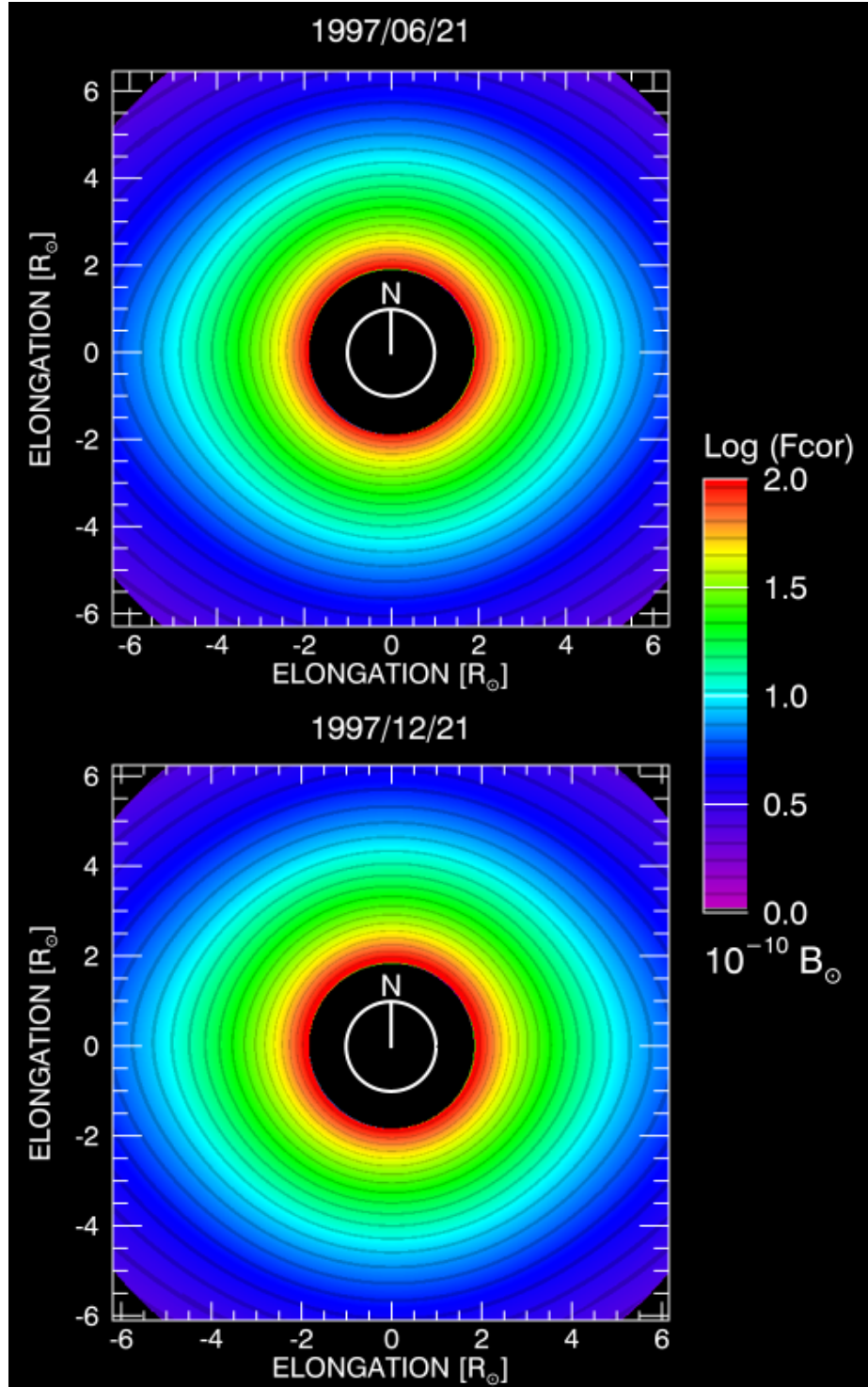


Figure 20. Two images of the F-corona produced by the restoration procedure described in Section 3.4 corresponding to the June (upper panel) and December (lower panel) 1997 nodes. The latter image is brighter than the former reflecting the effect of the varying Sun–SOHO distance, which is nearly minimal in December and nearly maximal in June of each year. Note the incidence on the elongation scale expressed in R_{\odot} .

3.5. Uncertainties Affecting the Restoration of the Stray Light and the F-Corona

As argued in Article I, the error analysis of data resulting from complex operations is extremely difficult, and even elaborated approaches such as Monte-Carlo error propagation are inapplicable. Ultimately, this led us to implement consistency checks and intercomparisons with several independent observations, prominently eclipse observations. Let us however develop several arguments in favor of the high accuracy of our restorations.

First of all, the starting set of “F+SL” images was indirectly validated by the extensive intercomparison between simultaneous C2 and eclipses images of the total radiance B and polarized radiance pB ; the agreement was generally so compelling that it allowed us to construct several composite images “eclipse + C2”. For instance, in the case of the eclipse of 26 February 1998, the circular profiles extracted from pB images obtained by C2 and by a team of the High Altitude Observatory (HAO) with their *Polarimetric Imager for Solar Eclipse 98* (POISE98) are in nearly perfect agreement except for a few local discrepancies that do not exceed 10 % (Figure 34 of Article I). The underlying assumption that the F-corona and the stray light are unpolarized, thus allowing their separation from the K-corona, is now further validated by a follow-on photopolarimetric analysis of the LASCO-C3 images in an article to be published shortly; it shows, in particular, that the assumption $p_F = 0$ holds at least out to $\approx 10 R_\odot$, well beyond the C2 field of view.

We showed above that, except for the diffraction fringe, it is quite difficult to disentangle the influence of the varying Sun–SOHO distance on the background stray light and on the F-corona. However, the modulation introduced by this variation remains modest, $\approx 15\%$ in the middle ring and $\approx 8\%$ in the outer ring (Figure 8), so that any error on this influence is certainly less than $\approx 2\%$.

Regarding the restoration of the stray-light images, tracking the errors along the various steps of the procedure is almost impossible, but general trends may be delineated. The diffraction fringe is so intense that it cannot be much affected by the underlying corona, as confirmed by its distinct variation with the Sun–SOHO distance. The large-scale background stray light is more challenging as it may be contaminated by remnants of the K-corona and a fraction of the F-corona. As already pointed out, the polarimetric separation had difficulties with bright K-corona structures, hence possible remnants, but they were efficiently removed by the multiple averaging steps in our procedure; indeed, the stray-light images do not exhibit structures reminiscent of the K-corona. Likewise, the large-scale spatial variations of the stray light are untypical of the smooth F-corona.

Regarding the restoration of the F-corona, a relevant point comes from the comparison of the equatorial profiles of the Fcor images scaled at 1 AU with that of the “K-L” model elaborated by Koutchmy and Lamy (1985). Indeed, the agreement is nearly perfect: the gradients are strictly similar and the absolute difference amounts to 6 %. It should be understood that this does not mean that our Fcor images are off by 6 % since the “K-L” model was obtained by analyzing and synthesizing various observations, which have their own uncertainties. It is

therefore a reasonable model, but its accuracy can certainly not be better than several percent. However, the above agreement offers a very valuable mutual validation.

As a final consistency check, we recombined the calculated stray light and the Fcor images and compared them with the original “F+SL” images. Four typical examples spanning the year 2002 (chosen at the peak activity of SC 23) are displayed in Figure 21. The histograms of the difference between the logarithm of the original and the restored images clearly indicate that the relative errors remain in the narrow range of $\pm 2\%$. As an additional feature, the ratios conspicuously reveal the remnants or residuals of the K-corona resulting from the imperfect polarization separation as mentioned in Section 3.1. Their contributions may be seen in the asymmetric tails of positive values in the above histograms and they do not exceed $\approx 5\%$.

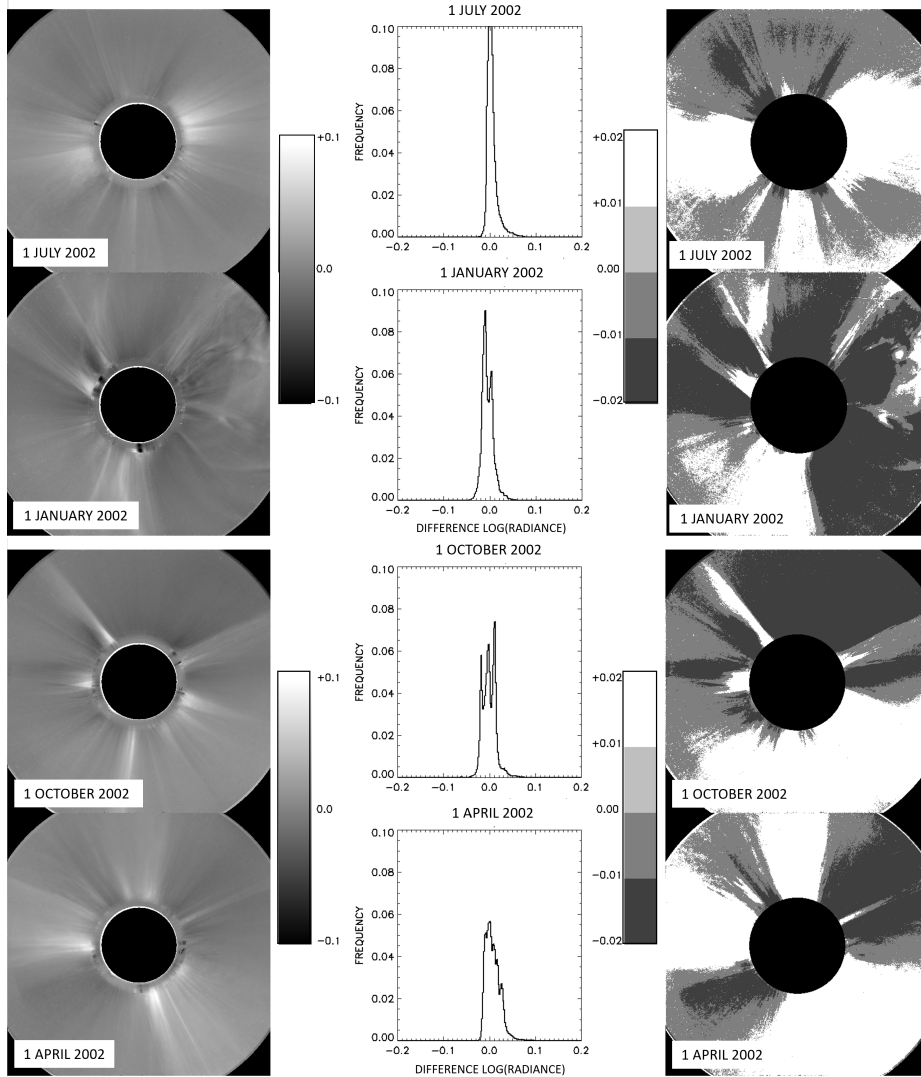


Figure 21. Illustrations of the ratio between the original “F+SL” images and the restored “Fcor+SL” images combining the calculated stray light and the Fcor images at four dates of 2002. In the upper two rows, the two dates correspond approximately to the times when the SOHO orbit crosses the plane of symmetry of the zodiacal cloud (the nodes). In the lower two rows, the two dates correspond approximately to the times when SOHO is at locations in quadrature with the nodes. Each panel is organized in three columns. The left columns display the logarithm of the ratios in the range -0.1 to +0.1. The right columns display regions where the logarithm of the ratios lies in four intervals defined by the gray bars. The central columns display the frequency distributions (histograms) of the difference between the logarithm of the original and the restored images.

4. Restoration of the K-Corona High Resolution Images

4.1. Restoration Procedure

With the images of the F-corona and of the stray light in hand, we are now in position to restore the K-corona from the routine, unpolarized, high-resolution images of 1024×1024 pixels by simple subtraction. C2 took these images at a cadence of typically 67 images per day until February 2009 and 118 images per day thereafter, except during two major interruptions mentioned in Section 2.1. This leads to a data set of 626,234 images at the end of 2019. As a matter of comparison, the respective numbers of the low resolution images of 512×512 pixels of the K-corona produced by the separation technique based on the analysis of polarization sequences (Lamy et al., 2020) are typically one image per day until February 2009 and four images per day thereafter for a total of 21,303 images. On the basis of the gain in spatial and temporal resolutions, it is expected that the subtraction approach will produce images of the K-corona suitable for improved tomographic reconstruction (Frazin et al., 2010). In addition, the polarimetric separation has inherent limitations resulting in the loss of some fraction of the K-corona signal. In other terms, this imperfect separation leaves some K-corona signal (i.e. residuals) in our “F+SL” images as mentioned in Section 3.4 and illustrated in Figure 21.

Our restoration procedure described below uses as input fully corrected and calibrated images generated by the routine pipeline processing developed at the Laboratoire d’Astrophysique de Marseille (formerly Laboratoire d’Astronomie Spatiale) as described in our past articles, notably Lamy et al. (2020). It corrects for all instrumental effects: bias, random errors in exposure times (Llebaria and Thernisien, 2001), missing telemetry blocks and impacts of cosmic rays (Pagot et al., 2014), and finally vignetting (Llebaria, Lamy, and Bout, 2004), and it applies a radiometric calibration to convert the raw data to units of $10^{-10} \overline{B}_{\odot}$. These corrections and the calibration are periodically updated as appropriate, thanks to a continuous monitoring of the in-flight performance of C2. The restoration procedure must take into account the temporal variation of the stray light and that of the F-corona as controlled by the heliocentric distance of SOHO, and with its roll. During its development and test, we discovered an additional problem with the centering of the images to be subtracted, which turns out to be critical since the K-corona is only a small fraction of the F-corona. For instance, at $5 R_{\odot}$, the ratios K/F of the radiances are typically 0.15 and 0.03 in the equatorial and polar directions, respectively. The centering problem arises from the fact that a slow drift of the center of the Sun as well as short-term fluctuations of typically a fraction of a pixel, but sometime up to a few pixels have been observed (Llebaria, Lamy, and Bout, 2004). Therefore, the F-corona image built from the Fourier series F_{cor} as described in Section 3.4 must be accurately re-centered before being subtracted. This was performed for each individual input image by considering its closest “F+SL” image, subtracting the “SL” image and performing a cross-correlation between the resulting “F” image and the daily F_{cor} images built from the Fourier series.

The formalism to restore an image of the K-corona $K(i, j, t)$ at any given time t from a corrected, high resolution, unpolarized image $I(i, j, t)$ may be conveniently expressed by the following equation:

$$K(i, j, t) = I(i, j, t) - C_{SL}(t) \times SL(i, j, t) / \mathcal{V}(i, j) - \text{Fcor}(i, j, t; i_0, j_0)$$

using the following definitions:

- $\mathcal{V}(i, j)$ is the C2 vignetting function,
- $\text{Fcor}(i, j, t; i_0, j_0)$ is the Fcor image built from the Fourier series and centered at (i_0, j_0) ,
- $C_{SL}(t)$ is a scaling coefficients applied to the stray-light images to account for the Sun-SOHO distance.

The procedure summarized by this expression is applied on an annual basis to limit the number of images to be processed in a single run. The different time scales and the embedding of the different terms require a practical organization as a set of nested operations with specific event rates to reset in proper order the needed auxiliary images and parameters as schematically represented in Figure 22. The five nested operations perform the following tasks:

- (a) Run the outermost loop over the input images controlled by the image index, which defines the absolute time t (Modified Julian Date).
- (b) Check the roll status of SOHO so as to specify the “SL” image.
- (c) Retrieve the appropriate daily Fcor image and the closest “F+SL” image updated one to four times per day depending upon the image cadence.
- (d) Re-center this Fcor image.
- (e) Generate the K-corona image according to the above equation.

4.2. Uncertainties Affecting the Restoration of the K-Corona

These uncertainties may be analysis on the basis of the above equation that expresses the K-corona $K(i, j, t)$. We first note that the vignetting function $\mathcal{V}(i, j)$ present in the second term does not introduce an additional uncertainty since it strictly compensates a first application of this function as explained in Section 2.3. Therefore, we are left with the uncertainties affecting the unpolarized images $I(i, j, t)$, which are controlled by the main operations applied to the raw images.

- Random errors in exposure times are corrected using an elaborated equalization procedure, particularly efficient in the case of the high-cadence unpolarized images, ensuring an accuracy better than 0.1 % (Llebaria and Thernisien, 2001).

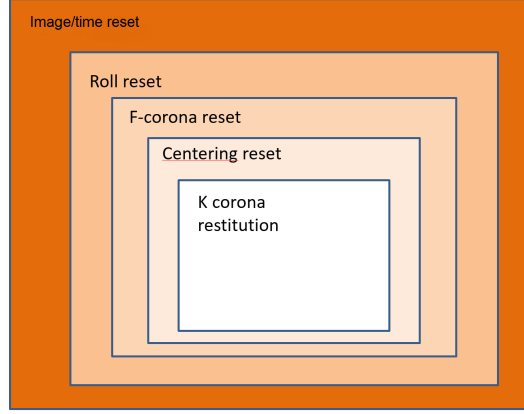


Figure 22. Schematic of the embedded operations implemented to generate the high-resolution images of the K-corona from the routine LASCO-C2 images.

- The vignetting function was obtained from a detailed modeling of the optics of C2 ensuring an accuracy better than 0.3 % (Llebaria, Lamy, and Bout, 2004).
- The absolute photometric calibration makes use of thousand of measurement of around a hundred stars so that the C2 calibration factor is determined with an accuracy better than 1 % (Lamy et al., 2020).

It can further be underlined that these operations were applied as well to the polarized images resulting in polarized radiance images in excellent agreement with various eclipse observations, thus offering an independent verification of their high photometric quality.

This error analysis of the terms of the above equation however misses a key aspect, which is unfortunately not amenable to a formal quantification: the critical centering of the Fcor images pointed out in Section 4, and which received special attention as described in this section. Figure 23 illustrates the marked effect on the restoration of a K-corona image of an offset of one pixel on the centering of an Fcor of 1024×1024 pixels. The resulting imbalance affecting the K-corona amounts to $\approx -4\%$ along the South direction and up to $\approx +8\%$ along the North direction. We are confident that the correlation procedure implemented in Section 4.1 ensures an optimal centering at the sub-pixel level. In summary, the above analysis indicates that the various uncertainties remain limited to at most a few percent, so that the global uncertainty affecting the high-resolution of the K-corona may be set at $\approx 10\%$, with possible accidental exceptions resulting for instance from imperfect centering of the images.

We very much regret the lack of images of the K-corona from ground-based, eclipse observations, thus precluding a direct comparison with our results as we performed for the pB images in Article I. As an alternative, we present in the next section relevant consistency checks by comparing various results on the radiance of the K-corona obtained by the two methods, subtraction (this work) and separation (Article I).

To conclude this section, we illustrate the importance of correctly assessing the background when retrieving the K-corona from the unpolarized LASCO-C2 images by comparing our results with those of Hayes, Vourlidas, and Howard (2001) already mentioned in the Introduction. We consider the same C2 image obtained on 26 February 1998 at 17:50 UT for which these authors provided two radial profiles, along the east equatorial and north polar directions as plotted in their Figure 3. Their “total brightness” denoted “ B ” is in fact the brightness of the K-corona obtained after subtracting a “background minimum model as an approximation to the F-corona”, thus ignoring any stray light. We extracted similar profiles from our K-image after applying a Lee filter so as to obtain the same smoothness as the Hayes *et al.*’s profiles. The differences plotted in Figure 24 are readily understood as resulting from the different “backgrounds”, being more pronounced in the case of the weaker polar profiles compared with the equatorial profiles. In both cases, the gradients are nearly similar up to $\approx 4 R_{\odot}$ and diverge beyond, consistent with the increasing role of the “background” with respect to the decreasing coronal signal. This is clearly seen on Hayes *et al.*’s polar profile, which exhibits a suspect turnover at $\approx 5.5 R_{\odot}$.

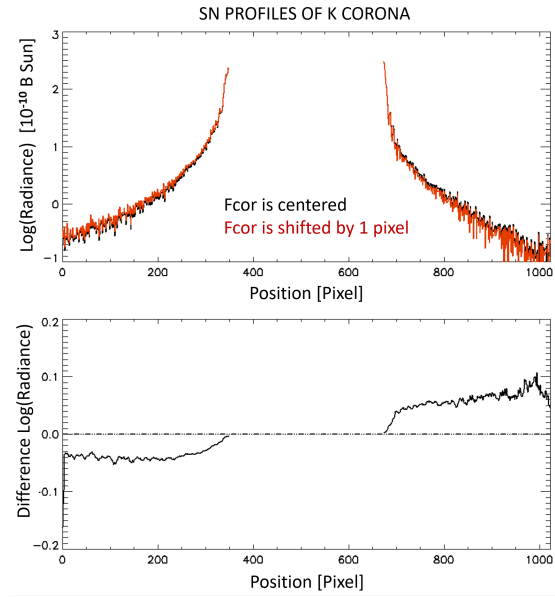


Figure 23. Illustration of the effect of a an offset of one pixel in the centering of the Fcor image on the restoration of the K-corona. The upper panel displays two North-South radiance profiles of the K-corona obtained with i) the properly centered Fcor image (black curve), and ii) the off-centered image by one pixel (red curve). The lower panel displays the difference of the logarithm of the two radiance profiles.

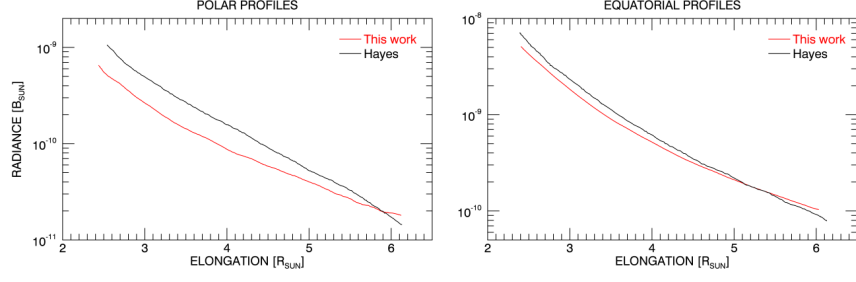


Figure 24. Comparison of the equatorial and polar profiles of the radiance of the K-corona on 26 February 1998 determined by Hayes, Vourlidas, and Howard (2001) (black curves) with those obtained with our restoration (red curves).

4.3. Comparison of the Restoration by Subtraction and by Separation

We now compare the radiance maps of the K-corona obtained by the two methods, subtraction and separation, limited to a few cases sampling SC 23 and 24 (Figure 25). This kind of display does not allow one to appreciate the gain in spatial resolution, but it does show the excellent agreement between the two methods. A few discrepancies are present in images obtained by subtraction but always in the innermost region, close to the diffraction fringe. This most likely reflects slight inaccuracies in the stray-light images and illustrates the difficulty of constructing these images to the finest detail. A quantitative comparison is offered by Figures 26 and 27 where equatorial, polar, and mean (averaged over 360°) profiles are compared. Both the radial gradients throughout the field of view and the radiance levels are in excellent agreement with only a few slight discrepancies. It is interesting to note that the South–North profiles of the K-corona by subtraction are noisier than their counterparts by separation in the outer part of the field of view and during times of low or reduced activity, precisely when the radiance reaches levels below $10^{-10} \overline{B_\odot}$.

4.4. Temporal Evolution of the Radiance of the K-corona

We finally compare the long-term temporal evolutions of the radiance of the K-corona obtained by the two methods: subtraction and separation. The radiance of the K-corona was globally integrated in an annular region extending from 2.7 to $5.5 R_\odot$ consistent with our past works, for instance Barlyaeva, Lamy, and Llebaria (2015). Taking into account the varying SOHO–Sun distance, the size of the inner and outer radii expressed in pixels varied accordingly to precisely measure the same region of the solar corona throughout the 24 years. The individual values of the integrated radiance were averaged over each Carrington rotation. We applied a slight smoothing by taking three-CR running means to allow easier comparison between the two curves, and we calculated the relative difference between them as displayed in Figure 28. The global agreement between the two evolutions is quite impressive, validating the inter-calibration of the two

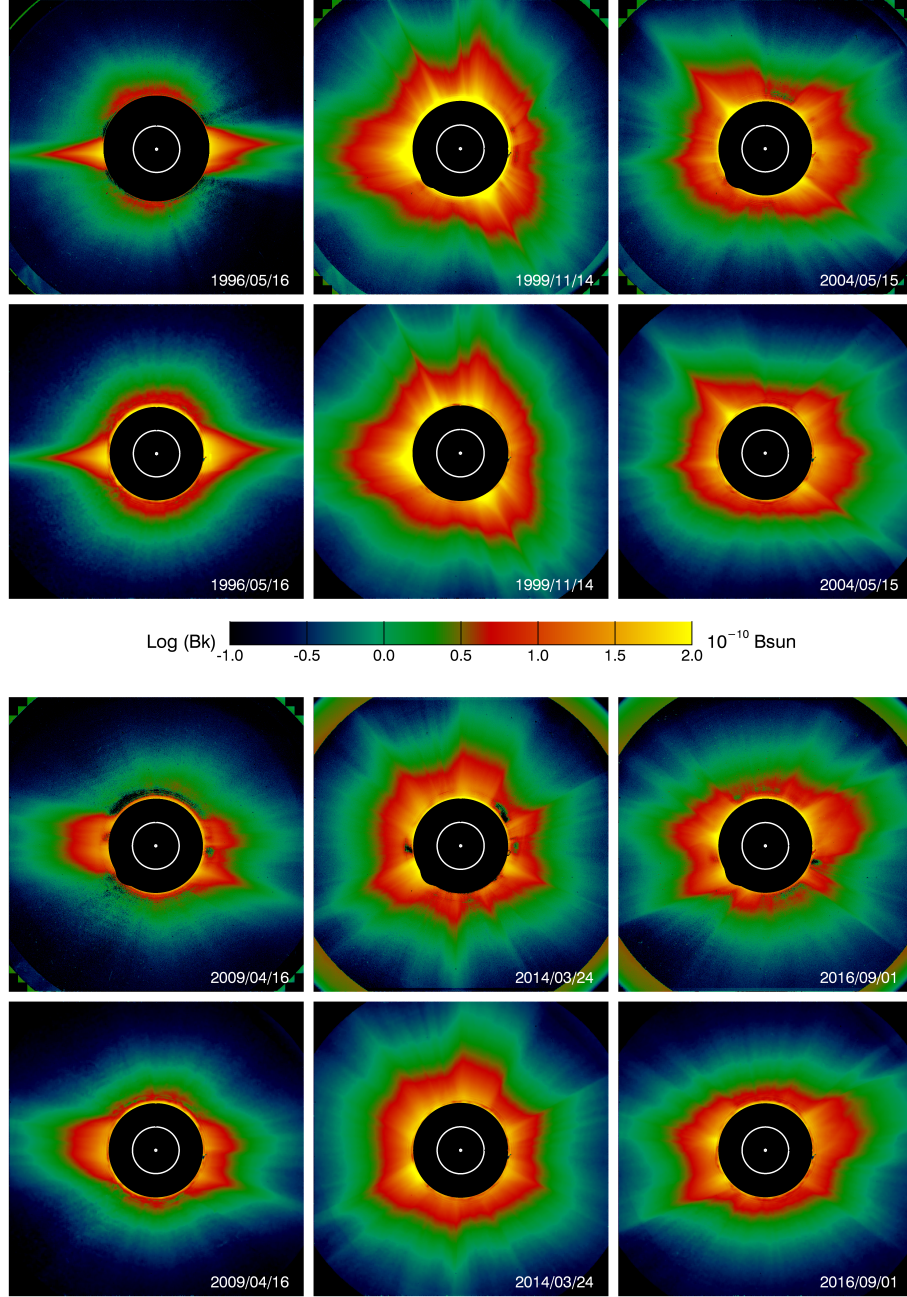


Figure 25. Comparison of the maps of the radiance of the K-corona sampling SC 23 (upper group of six images) and SC 24 (lower group of six images), and obtained by subtraction (upper rows of each group) and by separation (lower rows of group). The three columns correspond to three phases of activity of each cycle: minimum (left column), maximum (central column), and declining phases (right column). The dates are: 16 May 1996, 14 November 1999, and 15 May 2004 for SC 23 and 16 April 2009, 24 March 2014, and 1 November 2016 for SC 24. The white circles represent the solar disk and solar North is up.

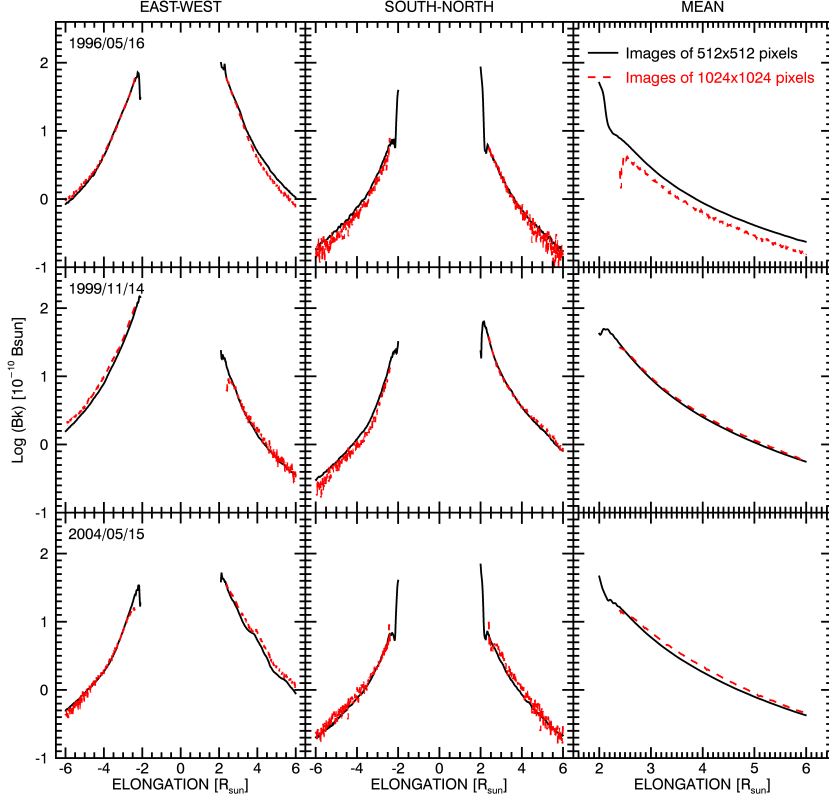


Figure 26. Comparison of the profiles of the radiance of the K-corona obtained by subtraction (red-dashed lines) and by separation (black lines) constructed from the maps shown in the upper panel of Figure 25 and corresponding to three phases of SC 23: 16 May 1996, 14 November 1999, and 15 May 2004. The radial profiles are displayed along the east–west (left column) and the south–north directions (central column), complemented by a mean profile (right column).

data sets as no scaling was introduced. The two curves track each other closely with a high degree of correlation of the short-term variations, thus demonstrating the consistency of the two methods of restoration of the K-corona, except for larger mismatches during the ascending phase of SC 24, which probably reflect the difficulty of accurately restoring the stray light. The relative difference (lower panel of Figure 28) has a global mean value of -2 %, but may be analyzed in terms of two regimes, incidentally corresponding to the two solar cycles although this may be fortuitous. From 1996 to 2010, the relative difference fluctuates about a mean value of -5 % with a standard deviation of 6 % whereas beyond 2010, the corresponding values are 2.3 % and 8 %, respectively. Still, they remain modest and fully demonstrate the validity of the two independent method of restoration of the K-corona.

The main features of the temporal evolution of the K-corona have already been investigated by our team, notably its solar cycle variation until 2014.5 and the presence of mid-term quasi-periodicities by Barlyaeva, Lamy, and Llebaria

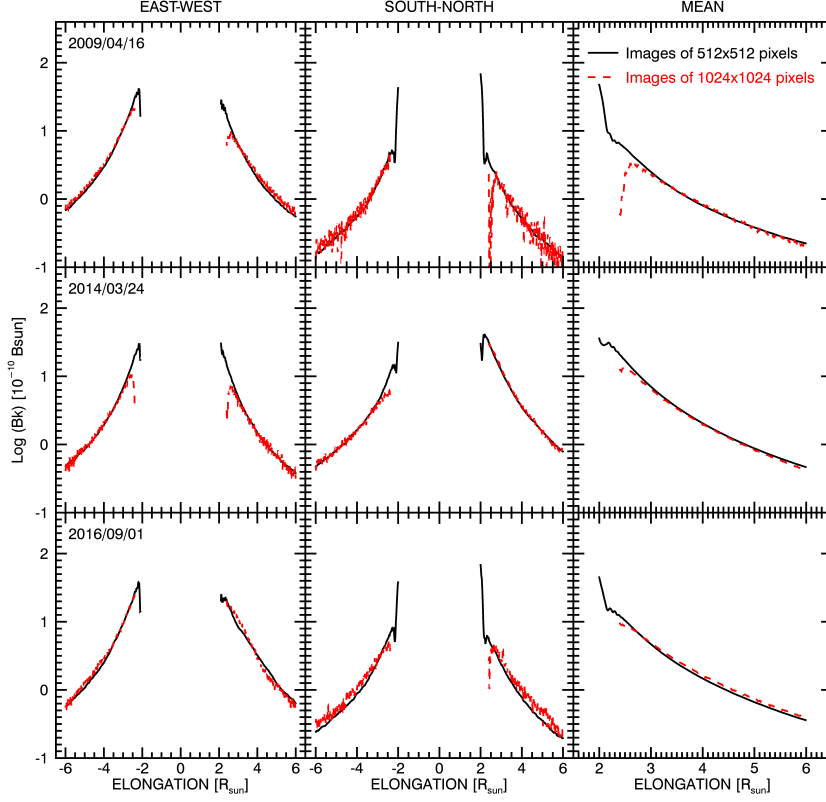


Figure 27. Comparison of the profiles of the radiance of the K-corona obtained by subtraction (red lines) and by separation (black lines) constructed from the maps shown in the lower panel of Figure 25 and corresponding to three phases of SC 24: 16 April 2009, 24 March 2014, and 1 November 2016. The radial profiles are displayed along the east–west (left column) and the south–north directions (central column), complemented by a mean profile (right column).

(2015), the comparison between the minima of Solar Cycles 22/23 and 23/24 by Lamy et al. (2014), and the anomalous surge at the end of 2014 by Lamy et al. (2017). We can now extend the comparison of minima to that of Solar Cycle 24/25 and make use of the data set resulting from the separation method since they are now available until mid-2020. Barlyaeva, Lamy, and Llebaria (2015) introduced several indices and proxies of solar activity to compare with the evolution of the radiance of the K-corona and also considered different latitudinal sectors. For brevity, we presently limit the comparison of the global K-corona integrated between 2.7 and 5.5 R_{\odot} with the total magnetic field (TMF) and the sunspot number (SSN). TMF was found to have the highest correlation with the K-corona whereas SSN has the lowest, but it is retained as the traditional indicator of solar (photospheric) activity. The SSN data come from the WDC-SILSO data center¹. The TMF data are calculated from the Wilcox Solar Observatory

¹<http://www.sidc.be/silso/datafiles>

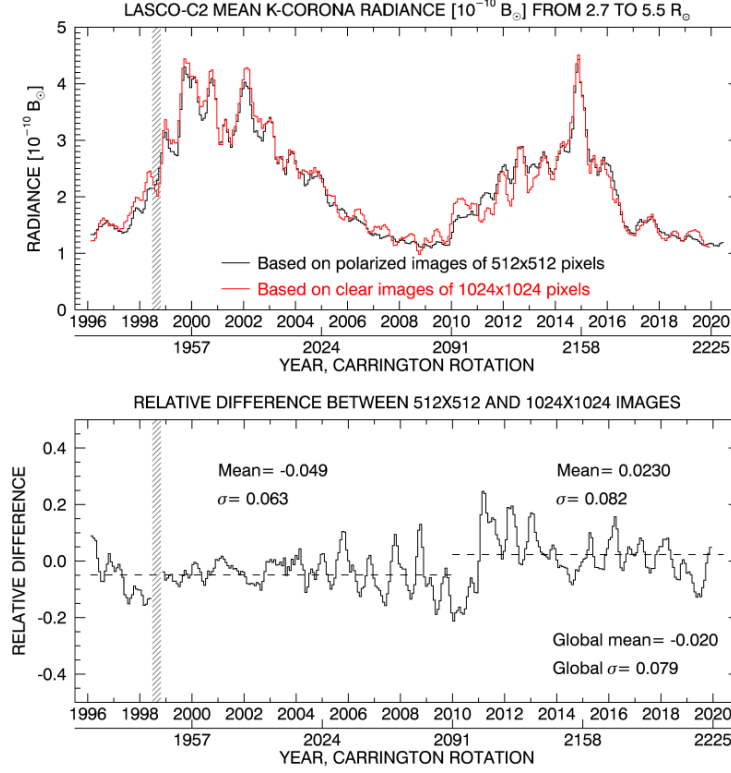


Figure 28. Upper panel: temporal variations of the global radiance of the K-corona integrated from 2.7 to 5.5 R_{\odot} . The two curves represent three-CR running means of the data averaged over the Carrington rotation. The black curve corresponds to the case of the images obtained by separation (512×512 pixels), and the red curve to the case of the images obtained by subtraction (1024×1024 pixels). Lower panel: relative difference between the two curves. The mean and standard deviation of the distributions are given for two time intervals and globally.

photospheric field maps by Y.-M. Wang according to a method developed by Wang and Sheeley (2003) and kindly made available to us. The time sampling of the comparison is the Carrington rotation as allowed by the TMF data in order to consider variations at the highest possible frequency. Figure 29 clearly confirms the conclusion of Barlyaeva, Lamy, and Llebaria (2015) that the variations of the K-corona radiance show a remarkably high correlation with the TMF at all timescales. The TMF also tracks to some extent the surge experienced by the corona in late 2014, which is not the case of the SSN since it is a purely photospheric index. Regarding the minimum of Solar Cycle 24/25, it is quite remarkable that the three data sets rigorously follow the same decreasing trend during the final years of the declining phase of SC 24, leveling off at the same low levels as those of the former “anomalous” SC 23/24 minimum. The subtle rising of the coronal radiance in early 2020, best seen on the smoothed profile (lower panel of Figure 29), marks the transition to SC 25 in agreement with the SSN data. In fact, correlating the two descending branches of SC 23 and 24

sets the duration of SC 24 at 11.0 years, precisely the value announced by the WDC-SILSO data center, i.e. the canonical duration of a solar cycle.

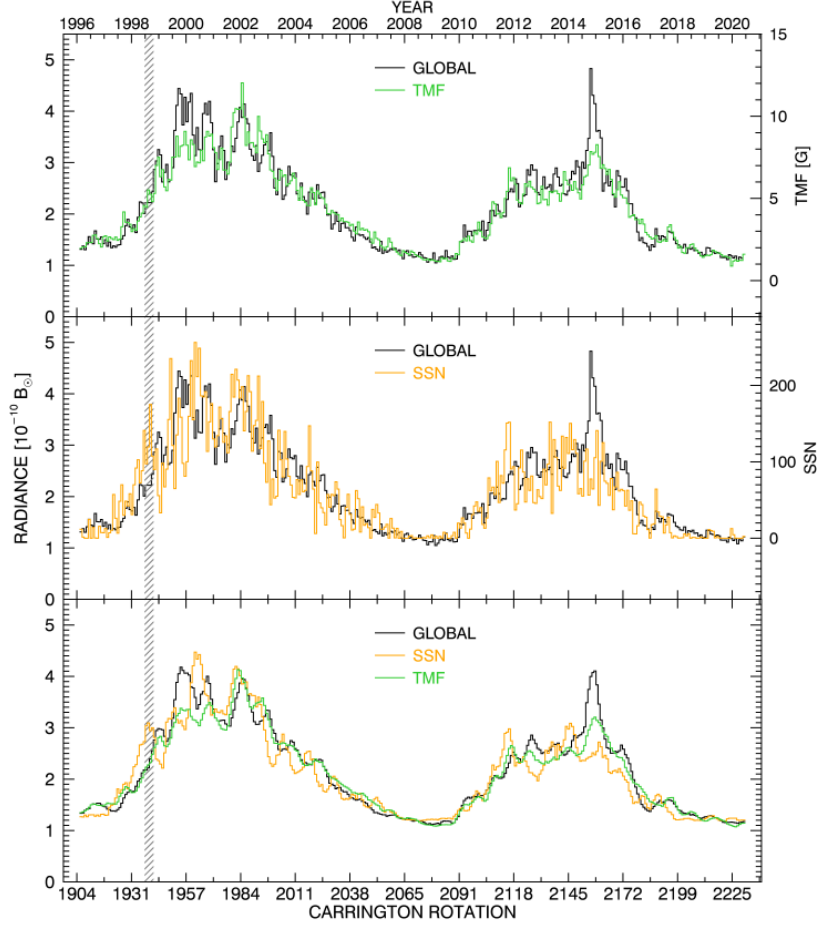


Figure 29. Comparison of the temporal variation of the global radiance of the K-corona integrated from 2.7 to 5.5 R_{\odot} with those of the total magnetic field (TMF) and the sunspot number (SSN). In the two upper panels, the time step is the Carrington rotation. In the lower panel, we applied a smoothing by taking five-CR running means to allow an easier comparison between the three curves.

5. Conclusion

In this article, we have presented the complex method developed to accurately determine the stray light and, in turn, the F-corona from the LASCO-C2 polarized images. This met our ultimate goal of the photometrically accurate restoration of the K-corona from the whole set of routine, high resolution images obtained over 24 Years [1996–2019], thus encompassing Solar Cycles 23 and

24. This achievement would have been impossible without the availability of the polarization sequences and their prior in-depth analysis, which allowed us to perform the crucial, initial extraction of the “F+SL” images (Lamy et al., 2020). It further benefited from the outstanding performances of C2, notably its sensitivity, its stability, and its very low level of stray light. However, our method – and this largely explains its complexity – had to cope with adverse conditions such as the impact of the loss of SOHO, periodic rolls, and the switch of orientation from solar North to ecliptic North. These changes are probably inevitable on long lasting space missions, but ultimately they did not hamper the photometric restoration over two solar cycles.

It is worth pointing out the excellent agreement between the two sets of images of the K-corona, that produced by polarimetric separation and that presently produced by subtraction of the F-corona and stray light. It however appears that the former method better handles the innermost region dominated by the bright diffraction fringe and more generally, the case of a faint K-corona characteristic of solar minima (Figure 25). This probably can be explained by the difficulty of performing an accurate restoration of the overwhelming stray light, which is the diffraction fringe, in this region. In addition, the subtraction method induces noisier images of the K-corona images than the separation, as clearly shown by the radial profiles of Figures 26 and 27. This has a simple explanation, as the noise affecting the F-corona (primarily shot noise) is transferred to the K-corona since we used a noiseless model of the F-corona. In principle, it could be eliminated or at least reduced by filtering as we implemented when we performed the comparison with the results of Hayes, Vourlidas, and Howard (2001). The above remarks tend to favor the polarimetric method provided it can be performed at a high spatial resolution and at a high cadence, an improvement that would also benefit to the three-dimensional reconstruction of CMEs based on their polarization. In that respect, advanced techniques as implemented at recent solar eclipses, such as micro-polarizer arrays affixed to the sensor (Burkpile et al., 2017; Vorobiev et al. 2017) should be considered for future space coronagraphs. This should lead to more photometrically accurate maps of the K-corona as well as of the polarized radiance pB . However, if one is interested in characterizing the F-corona, accurate subtraction of the stray light remains to be confronted.

Concerning the implications for the K-corona observed over two solar cycles, we have confirmed that the temporal variation of the integrated radiance of the K-corona closely tracks the solar activity, and that it is highly correlated with the temporal variation of the total magnetic field. We have further found that the behaviours of the integrated radiance during the last few years of the declining phases of Solar Cycles 23 and 24 are remarkably similar, reaching the same base level and leading to a duration of 11.0 years for the latter cycle, in agreement with the value from the sunspot number series. Concerning the F-corona, we have revealed a long-term evolution of its radiance that clearly does not follow the solar cycle and this suggests a secular variation intrinsic to the inner zodiacal cloud. This will be further explored in a forthcoming article that will combine the observations by both C2 and C3.

The complete data set of the reconstructed high resolution images of the K-corona (FITS files) as well as the set of daily “Fcor” images are available from the LASCO-C2 Legacy Archive² hosted at the Integrated Data and Operation Center (formerly MEDOC) of the Institut d’Astrophysique Spatiale. The K-corona images may be conveniently visualized thanks to a set of pages, each one regrouping 24 compressed images at the format of 256×256 pixels. Each image is labeled with the original name of the source image and with the time expressed in “yyyy/mm/dd hh:mm:ss” and in MJD–50,000, where MJD is the Modified Julian Date. The radiance of the K-corona is displayed in units of $10^{-10} \overline{B}_{\odot}$ using a logarithmic scale. Each group of 24 consecutive images arranged in a 6×4 format in lexicographical order from bottom to top is presented in a page. Each page is identified by its name which incorporates the date (yyyymmdd) and time T (hhmm) of the last image, followed by the date expressed in MJD (without the decimal point), for example “map_20030905_1030_528874”. A color bar is placed at the center of each page. Figure 30 displays an example of such a page. The set of pages covering a month of observation (typically 120 pages) is regrouped in a document in PDF format. For the first 24 years of operation, there are 284 documents since four months are missing due to the loss of SOHO. These PDF documents are accessed via a dedicated table where the entries are year and month.

Acknowledgments We thank Y.-M. Wang for providing the Total Magnetic Field (TMF) data. The LASCO-C2 project at the Laboratoire d’Astrophysique de Marseille and the Laboratoire Atmosphères, Milieux et Observations Spatiales is funded by the Centre National d’Etudes Spatiales (CNES). LASCO was built by a consortium of the Naval Research Laboratory, USA, the Laboratoire d’Astrophysique de Marseille (formerly Laboratoire d’Astronomie Spatiale), France, the Max-Planck-Institut für Sonnensystemforschung (formerly Max Planck Institute für Aeronomie), Germany, and the School of Physics and Astronomy, University of Birmingham, UK. SOHO is a project of international cooperation between ESA and NASA.

Disclosure of Potential Conflicts of Interest The authors declare that they have no conflicts of interest.

References

- Barlyaeva, T., Lamy, P., Llebaria, A.: 2015, Mid-Term Quasi-Periodicities and Solar Cycle Variation of the White-Light Corona from 18.5 Years (1996.0 - 2014.5) of LASCO Observations. *Solar Phys.* **290**, 2117. DOI. ADS.
- Battams, K., Howard, R.A., Dennison, H.A., Weigel, R.S., Lean, J.L.: 2020, The LASCO Coronal Brightness Index. *Solar Phys.* **295**, 20. DOI. ADS.
- Brueckner, G.E., Howard, R.A., Koomen, M.J., Korendyke, C.M., Michels, D.J., Moses, J.D., Socker, D.G., Dere, K.P., Lamy, P.L., Llebaria, A., Bout, M.V., Schwenn, R., Simnett, G.M., Bedford, D.K., Eyles, C.J.: 1995, The Large Angle Spectroscopic Coronagraph (LASCO). *Solar Phys.* **162**, 357. DOI. ADS.

²<http://idoc-lasco-c2-archive.ias.u-psud.fr>

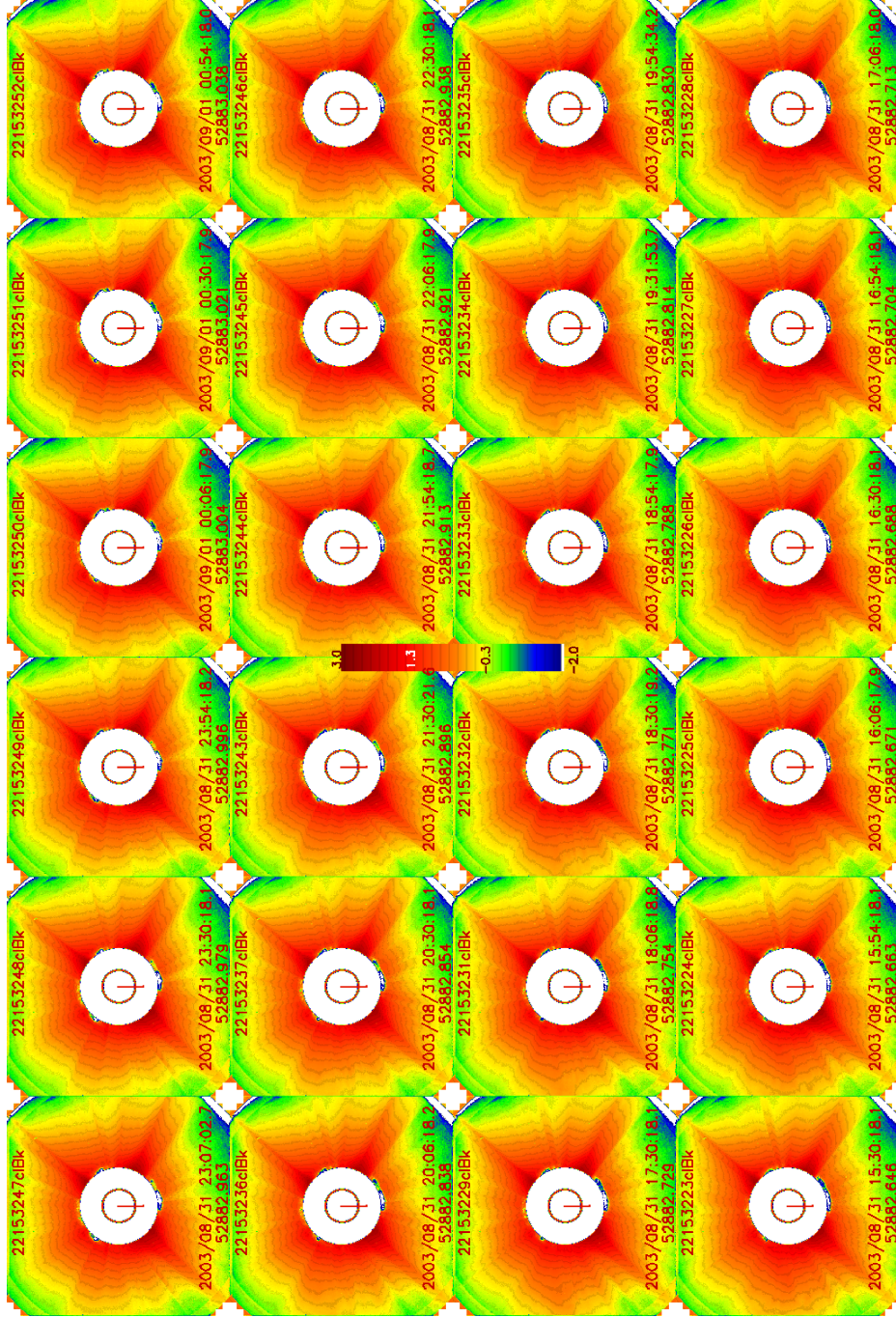


Figure 30. An example of a page displaying 24 images of the reconstructed K-corona from the LASCO-C2 Legacy Archive.

- Burkepile, J., Boll, A., Casini, R., de Toma, G., Elmore, D.F., Gibson, K.L., Judge, P.G., Mitchell, A.M., Penn, M., Sewell, S.D., Tomczyk, S., Yanamandra-Fisher, P.A.: 2017, Polarization Observations of the Total Solar Eclipse of August 21, 2017. *AGU Fall Meeting Abstr.* ADS.
- Dolei, S., Spadaro, D., Ventura, R.: 2016, Mapping the coronal hydrogen temperature in view of the forthcoming coronagraph observations by Solar Orbiter. *Astron. Astrophys.* **592**, A137. DOI. ADS.
- Domingo, V., Fleck, B., Poland, A.I.: 1995, The SOHO Mission: an Overview. *Solar Phys.* **162**, 1. DOI. ADS.
- Fainshtein, V.G.: 2007, Some properties of the latitude brightness distributions in the K and F coronae according to SOHO/LASCO data. *Astron. Rep.* **51**, 1026. DOI. ADS.
- Fainshtein, V.G.: 2009, New method for separating K- and F-corona brightness based on LASCO/SOHO data. *Geomagn. Aeron.* **49**, 830. DOI. ADS.
- Frazin, R.A., Lamy, P., Llebaria, A., Vázquez, A.M.: 2010, Three-Dimensional Electron Density from Tomographic Analysis of LASCO-C2 Images of the K-Corona Total Brightness. *Solar Phys.* **265**, 19. DOI. ADS.
- Hayes, A.P., Vourlidas, A., Howard, R.A.: 2001, Deriving the Electron Density of the Solar Corona from the Inversion of Total Brightness Measurements. *Astrophys. J.* **548**, 1081. DOI. ADS.
- Koutchmy, S., Lamy, P.L.: 1985, The f-corona and the circum-solar dust evidences and properties. In: Giese, R.H., Lamy, P. (eds.) *IAU Colloq. 85: Properties and Interactions of Interplanetary Dust*, *Astrophys. Space Sci. Lib.* **119**, 63. DOI. ADS.
- Lamy, P., Barlyaeva, T., Llebaria, A., Floyd, O.: 2014, Comparing the solar minima of cycles 22/23 and 23/24: The view from LASCO white light coronal images. *J. Geophys. Res.* **119**, 47. DOI. ADS.
- Lamy, P., Boclet, B., Wojak, J., Vibert, D.: 2017, Anomalous Surge of the White-Light Corona at the Onset of the Declining Phase of Solar Cycle 24. *Solar Phys.* **292**, 60. DOI. ADS.
- Lamy, P., Llebaria, A., Boclet, B., Gilardy, H., Burtin, M., Floyd, O.: 2020, Coronal Photopolarimetry with the LASCO-C2 Coronagraph over 24 Years [1996 - 2019] – Application to the K/F Separation and to the Determination of the Electron Density. *Solar Phys.* **295**, 89. DOI. ADS.
- Leinert, C., Grun, E.: 1990, In: Schwenn, R., Marsch, E. (eds.) *Interplanetary Dust*, Springer-Verlag, Berlin, Heidelberg, New York, 207. ADS.
- Leinert, C., Richter, I., Pitz, E., Planck, B.: 1981, The zodiacal light from 1.0 to 0.3 A.U. as observed by the HELIOS space probes. *Astron. Astrophys.* **103**, 177. ADS.
- Llebaria, A., Thernisien, A.: 2001, Highly accurate photometric equalization of long sequences of coronal images. In: *Astronomical Data Analysis* **4477**, 265. International Society for Optics and Photonics. DOI.
- Llebaria, A., Lamy, P., Bout, M.: 2004, Lessons learnt from the soho lasco-c2 calibration. In: *Proc. SPIE* **5171**, 27. DOI.
- Llebaria, A., Lamy, P., Koutchmy, S.: 1999, The Global Activity of the Solar Corona. In: Vial, J.-C., Kaldeich-Schü, B. (eds.) *8th SOHO Workshop: Plasma Dynamics and Diagnostics in the Solar Transition Region and Corona*, *ESA SP-446*, 441. ESA, Noordwijk. ADS.
- Llebaria, A., Loirat, J., Lamy, P.: 2012, In-orbit determination of the straylight in the SOHO/LASCO-C2 coronagraph and its temporal evolution. In: Clampin, M.C., Fazio, G.G., MacEwen, H.A., Oschmann, J. Jacobus M. (eds.) *Space Telescopes and Instrumentation 2012: Optical, Infrared, and Millimeter Wave*, *Proc. SPIE* **8442**, 844226. DOI. ADS.
- Morgan, H., Habbal, S.R.: 2007, The long-term stability of the visible f corona at heights of 3 to 6 solar radii. *Astron. Astrophys.* **471**, L47.
- Munro, R.H., Jackson, B.V.: 1977, Physical properties of a polar coronal hole from 2 to 5 solar radii. *Astrophys. J.* **213**, 874. DOI. ADS.
- Pagot, E., Lamy, P., Llebaria, A., Boclet, B.: 2014, Automated processing of lasco coronal images: Spurious point-source-filtering and missing-blocks correction. *Solar Phys.* **289**, 1433. DOI.
- Quémerais, E., Lamy, P.: 2002, Two-dimensional electron density in the solar corona from inversion of white light images-application to soho/lasco-c2 observations. *Astron. Astrophys.* **393**, 295. DOI.
- Saito, K., Poland, A.I., Munro, R.H.: 1977, A study of the background corona near solar minimum. *Solar Phys.* **55**, 121.
- Stenborg, G., Howard, R.A.: 2017, The Evolution of the Surface of Symmetry of the Interplanetary Dust from 24° to 5° Elongation. *Astrophys. J.* **848**, 57. DOI. ADS.

- Van de Hulst, H.C.: 1947, Zodiacal Light in the Solar Corona. *Astrophys. J.* **105**, 471. DOI. ADS.
- Von Klüber, H.: 1958, Intensities, polarization and electron density of the solar corona from photographs taken at the total solar eclipse of 1952 february 25. *Mon. Not. Roy. Astron. Soc.* **118**, 201.
- Vorobiev, D., Ninkov, Z., Bernard, L., Brock, N.: 2017, Imaging polarimetry of the 2017 solar eclipse with the rit polarization imaging camera. *arXiv:1710.04255*.
- Wang, Y.-M., Sheeley, N.R.: 2003, On the Fluctuating Component of the Sun's Large-Scale Magnetic Field. *Astrophys. J.* **590**, 1111. DOI. ADS.